



Tungsten solubility and speciation in hydrothermal solutions revealed by in situ X-ray absorption spectroscopy

Manuela Borchert^{1,2}, Maria A. Kokh^{1,3}, Marion Louvel^{1,4}, Elena F. Bazarkina^{5,6}, Anselm Loges⁷, Edmund Welter², Denis Testemale⁸, Rami Al Abed³, Stephan Klemme¹, and Max Wilke³

¹Institut für Mineralogie, Universität Münster, Corrensstrasse 24, 48149 Münster, Germany

²Deutsches Elektronen-Synchrotron DESY, Notkestrasse 85, 22607 Hamburg, Germany

³Institut für Geowissenschaften, Universität Potsdam, Karl-Liebknecht-Str. 24–25, 14476 Potsdam, Germany

⁴Institut des Sciences de la Terre d'Orléans, CNRS–BRGM–Univ. Orléans,
1A rue de la Ferrollerie, 45100 Orléans, France

⁵Institute of Resource Ecology, Helmholtz-Zentrum Dresden-Rossendorf (HZDR),
P.O. Box 510119, 01314 Dresden, Germany

⁶The Rossendorf Beamline, European Synchrotron Radiation Facility (ESRF),
CS40220, 38043 Grenoble CEDEX 9, France

⁷Institut für Geologische Wissenschaften, Freie Universität Berlin, Malteserstr. 74–100, 12249 Berlin, Germany

⁸Université Grenoble Alpes, CNRS, Institut Néel, 38000 Grenoble, France

Correspondence: Max Wilke (wilkem@uni-potsdam.de)

Received: 2 June 2024 – Revised: 18 December 2024 – Accepted: 25 December 2024 – Published: 26 February 2025

Abstract. Tungsten (W) concentrations in fluids in equilibrium with crystalline tungsten oxide are used to determine thermodynamic parameters for W solubility and W species in hydrothermal fluids. The solubility data were measured in situ at high pressures and temperatures using X-ray absorption. X-ray spectroscopic data measured in situ – with X-ray absorption near-edge structure (XANES) and extended X-ray absorption fine structure (EXAFS) – were applied to characterize the symmetry and the type of atoms of the first coordination shell of W aqueous complexes present in the fluid at given temperatures and pressures. Experiments were performed at up to 400 °C and at pressures of 40, 50 and 60 MPa. With this dataset, we were able to improve constraints for the already-suggested fluid species WO_4^{2-} , HWO_4^- , H_2WO_4^0 , NaWO_4^- and NaHWO_4^0 . Further, we were able to introduce the H_3WO_4^+ species that is found to be dominant in acidic fluids. No evidence was found for W species involving Cl^- as a ligand. The ionic W species found in the fluid are characterized by a tetrahedral complex at alkaline conditions. In neutral to acidic conditions, W complexes with distorted octahedral symmetry are formed. These complexes may be polymerized at temperatures ≤ 200 °C and W concentrations $> 10^{-3}$ mol kg⁻¹ H₂O. X-ray spectroscopy as well as thermodynamic modeling suggests that polytungstate species are not relevant at equilibrium concentrations found in the solubility experiments of this study ($\leq 10^{-3}$ mol W kg⁻¹ H₂O in equilibrium with tungsten oxide) or at concentrations reported for natural systems. Using the thermodynamic properties of the species mentioned above, in situ data on the solubility of scheelite can be successfully described. Thermodynamic modeling shows that scheelite solubility and wolframite solubility strongly increase with increasing salinity, especially up to 1 m NaCl (*m* denotes molality), and vary with pH, which is consistent with earlier reports. Overall, this study provides improved thermodynamic properties for a set of W fluid species that cover a wide range of fluid compositions, which is necessary for understanding the complex processes of W enrichment and mineralization in hydrothermal systems.

1 Introduction

Hydrothermal ore deposits are the main source of many critical elements, and it is commonly accepted that these deposits are formed from aqueous fluids at crustal pressures and temperature (Seward, 1981; Crerar et al., 1985; Seward and Barnes, 1997; Brugger et al., 2016). Tungsten (W) is one of these critical metals (Klimek et al., 2015), and its outstanding chemical and physical properties (e.g., high melting point, high corrosive resistance and tensile strength) ensure that W-rich alloys are ubiquitous in high-tech industrial applications. Low-grade W deposits are common worldwide, but only a few global provinces host world-class W deposits of economic importance, e.g., Xihuashan (China), Hemerdon (UK), Mt. Pleasant (Canada), Panasqueira (Portugal), Felbertauern (Austria), Barruecopardo (Spain) or Dzhida (Russia) (e.g., Han et al., 2021, and references therein). The main W-bearing minerals in these deposits are the tungstate minerals scheelite, CaWO_4 , and wolframite, $(\text{Fe,Mn})\text{WO}_4$. These minerals are commonly formed in close association with granitoid plutons (e.g., Wood and Samson, 2000; Lecumberri-Sanchez et al., 2017; Korges et al., 2018). Tungsten occurs in the Earth's crust preferentially in hexavalent state, and according to the Pearson (1963) classification, W^{6+} is a hard cation. As such, it tends to hydrolyze water molecules to form stable and soluble anionic tungstate species, e.g., WO_4^{2-} , that may form ion pairs with Na^+ , K^+ or H^+ in hydrothermal aqueous fluids (e.g., Rafal'sky et al., 1984; Heinrich, 1990; Gibert et al., 1992; Wood and Samson, 2000; Lecumberri-Sanchez et al., 2017). The fact that W is transported as anionic species and is not usually found as an oxide phase in nature implies that Ca, Fe or Mn, the main cations in ore-forming scheelite and wolframite, can only be minor components in fluids transporting W. These ore minerals are then probably formed as a consequence of fluid–fluid mixing or fluid–rock interaction, where concentrations of Ca, Fe or Mn are increased to meet the solubility of wolframite or scheelite. Lecumberri-Sanchez et al. (2017) studied fluid inclusions and host-rock chemistry of the Panasqueira W deposit. Their data show that the host-rock chemistry controls the type of wolframite mineralization in schists and hornfels; i.e., fluid–rock interaction leads to muscovitization and/or tourmalinization in the host rocks. Subsequently, Fe is released from the rock into the fluid, which leads to precipitation of wolframite. A similar process has been proposed for scheelite deposits in skarns (Kwak, 1987; Ordosch et al., 2019). Ordosch et al. (2019) assign the formation of W–Sn skarns close to the world-class Felbertal scheelite deposit (Austria) to the reaction of hydrothermal fluids with amphibolite host rocks. Scheelite mineralization in the Felbertal deposit itself is associated with quartz veins within a metamorphosed ophiolite to arc sequence, and the W-carrying hydrothermal fluids were related to highly evolved magmas

(Kozlik and Raith, 2017). Zhang et al. (2018) studied the role of hydrothermal alteration of the host rock in W mineralization at the Dahutang tungsten deposit (China) and showed that W mineralization is associated with superimposed alkaline alteration. Three hydrothermal alteration stages were identified, and W mineralization occurs in all stages independently of fluid chemistry, albeit at very different grades (Zhang et al., 2018). The most important alteration is associated with an acidic to strongly acidic fluid (reducing $f\text{O}_2$, 440 to 160 °C). Here, greisen and silicic alteration occur and scheelite and wolframite are precipitated, with a bulk rock W concentration of $7300 \mu\text{g g}^{-1}$. Thus, economically significant W mineralization seems to be correlated with lowering of the pH of the fluid that transports W, which at the same time interacts with host-rock minerals to provide a source of Ca, Fe or Mn to facilitate formation of tungstate minerals.

For a comprehensive understanding and development of geochemical models for W hydrothermal ore deposit genesis, it is necessary to measure W solubility and speciation experimentally in different fluid compositions and at different pH, pressures and temperatures. The experimental data may then be used to develop thermodynamic models of W speciation and W solubility. Pioneering studies by Wood and Samson (2000) suggest that scheelite and wolframite solubility can reach several thousands of $\mu\text{g g}^{-1}$ in fluids at $200 < T < 500$ °C and $20 < P < 150$ MPa. They concluded that H_2WO_4^0 , HWO_4^- , WO_4^{2-} and alkali-tungstate ion pairs are the species in the fluid compositions studied and that complexation with Cl, F or carbonate ions was less likely (Wood and Samson, 2000). Furthermore, their thermodynamic model shows that W solubility increases with temperature and pH. More recent solubility experiments by Wang et al. (2019, 2020a) confirmed that WO_3 solubility is mainly controlled by T and pH and remains unaffected by Cl concentrations at temperatures between 250 and 350 °C. Based on these measurements, Wang et al. (2019) proposed that H_2WO_4^0 is the dominant species at $\text{pH}(T) < 2.8$ and HWO_4^- is the dominant species up to a $\text{pH}(T)$ of 5 (200 °C). At higher $\text{pH}(T)$, they proposed WO_4^{2-} as the dominant W species. Raman measurements made in situ (Carocci et al., 2022) in silica capillaries further established that, while polymeric tungstate species (also called polynuclear complexes) may be stable at low temperature and under very acidic conditions, W is mostly present as the monomeric species WO_4^{2-} , HWO_4^- , H_2WO_4^0 and alkali-tungstate ion pairs at temperatures above 300 °C. Raman spectroscopy also showed that W does not form any stable carbonate complexes up to 400 °C and 60 MPa (Wang et al., 2020b; Carocci et al., 2022). The latest study on W speciation (Mei et al., 2024) combined ab initio molecular dynamics with X-ray absorption near-edge structure (XANES) and extended X-ray absorption fine structure (EXAFS) at high pressure and temperature, addressing the W species in F-, S- and NaCl-bearing

solutions. In S- and F-free NaCl-bearing systems, they confirm observations by Carocci et al. (2022), whereas replacement of O by F or S was observed for F- and S-bearing solutions.

The experiments of Wang et al. (2019) as well as the older studies on W solubility in hydrothermal solutions were quench experiments. These experiments, even if performed carefully, may be affected by uncertainties that originate from the quench process due to precipitation or back reaction of fluid and solid during or after quenching. Studies at high pressure and temperature on W were performed in situ by Raman spectroscopy only. These were useful in assigning W species present in the fluid, but the results are difficult to quantify in terms of solubility due to the unknown cross-sections of the Raman bands. There is spectroscopic evidence in the literature that W species under acidic conditions have very different molecular symmetry compared to alkaline conditions (e.g., Hoffmann et al., 2000; Wang et al., 2020a; Carocci et al., 2022). This implies stoichiometry that is different from the tungstate anion (WO_4^{2-}). Further, formation of polytungstates has been reported, particularly at low pH, but it has not been unequivocally documented whether these species are relevant to natural systems at high pressure and temperature. Finally, it remains unclear whether oxygen ligands may be replaced by Cl^- at high temperature and/or very low pH, as has been reported for Mo (Borg et al., 2012). To address these matters, we present in situ X-ray spectroscopic data for W solubility and W speciation in various hydrous fluids (H_2O , HCl and NaCl solution) from 100 to 400 °C and 40 or 50 MPa. In the experiments, W-oxides and synthetic scheelite were equilibrated with different hydrothermal solutions and measurements were performed using a hydrothermal autoclave and X-ray absorption spectroscopy (Testemale et al., 2005, 2024; Klemme et al., 2021). We compare the concentrations determined in situ at high pressure and temperature to existing and newly developed thermodynamic models that describe W solubility in aqueous fluids under conditions relevant to hydrothermal ore formation.

2 Experimental and analytical methods

2.1 Sample preparation

CaWO_4 and WO_3 were purchased from Alfa Aesar (p.a. 99.9 % each) and pressed into pellets 13 mm in diameter. These pellets were sintered at 1030 °C in air for ~ 16 h to improve the mechanical stability in solution. $\text{WO}_{2.7}$ oxide, which is the thermodynamically stable phase in the presence of graphite in our experiments, was prepared from WO_3 by sintering pressed pellets at 1030 °C for ~ 16 h in a gas that consisted of Ar + 5 % H_2 saturated with H_2O vapor at room temperature to buffer the H_2O fugacity. The compositions of all starting materials were confirmed by powder X-ray diffraction (XRD). Aqueous solutions were produced

by weight from de-ionized water and analytical-grade powders of NaCl or 30 vol % hydrochloric acid. Solutions for analysis of the extended X-ray absorption fine structure (EXAFS) data in the absence of a solid phase were prepared from analytical-grade powder of $\text{Na}_2\text{WO}_4 \cdot 2\text{H}_2\text{O}$ dissolved in different aqueous solutions.

2.2 Hydrothermal autoclave

Experiments performed in situ were carried out in dedicated hydrothermal autoclaves at beamlines P65 (PETRA III, DESY, Hamburg, Germany) and BM30 (FAME, European Synchrotron Radiation Facility (ESRF), Grenoble, France). The design and functionality of both autoclaves are similar, and details are given in Testemale et al. (2005, 2016, 2024) and Klemme et al. (2021). Briefly, the samples, either an aqueous solution or a sintered pellet + aqueous solution, were loaded into a vitreous carbon tube. Two freely moveable pistons, also made from vitreous carbon, confined the fluid within the tube. The loaded vitreous carbon cell was placed inside a heater assembly, and this assembly was inserted into the stainless-steel autoclave. The experiments were started by removing a small amount of remaining air from the autoclave, and subsequently the autoclave was pressurized to the desired experimental pressure, i.e., at 40, 50 or 60 MPa, using He gas as the pressure-transmitting medium. The samples were heated using a resistive wire heater (ESRF BM30: 0.1 mm Mo wire; DESY P65: 0.1 mm stainless-steel wire), and temperatures were measured with two N-type (Nicrosil–Nisil) thermocouples placed at either end of the furnace, i.e., above and below the X-ray windows. For each heater assembly, a T calibration, which was based on the density of pure water, was performed before the experimental series. The offset between the T measured at the thermocouples and the actual T of the sample was calculated by determining the X-ray absorption of pure water at 40, 50 or 60 MPa and 20, 50, 100, 150, 200, 250, and 300 °C at an energy level of 10.1 keV, and these results were compared to the pure-water density values taken from the NIST Chemistry WebBook (Lemmon et al., 2019). Values for X-ray absorption cross-sections of water were taken from Elam et al. (2002). The accuracy of overall T determination is estimated to be < 5 °C at 25 °C and ~ 10 °C at 300 °C for each heater assembly used during all the experimental sessions.

2.3 Beamlines and spectrum acquisition

The EXAFS beamline P65 (PETRA III) applied consists of a short 11-period undulator device, two water-cooled plane mirrors with different coatings (Si, Rh, Pt) and a water-cooled double-crystal monochromator (DCM, (Si111) or (Si311)). The key parameters of the P65 beamline are a working range of 4–44 keV, a photon flux of up to 1×10^{12} photons s^{-1} (at 9 keV) and an energy resolution ($\Delta E/E$) of 1.4×10^{-4} for Si (111) DCM. The beam size

at the sample is $1 \text{ mm} \cdot 0.5 \text{ mm}$ ($h \cdot v$) and can be adjusted by a slit system located in front of the first ionization chamber (I0). A detailed description of the beamline can be found in Welter et al. (2019). The French Absorption spectroscopy beamline in Material and Environmental science BM30 (FAME, ESRF) consists of a bending magnet (0.8 T), a water-cooled Rh-coated Si mirror, a double-crystal monochromator (Si (220)) with a nitrogen-cooled first crystal and a bendable second crystal for horizontal focusing, and a second Rh-coated Si mirror for vertical focusing. The photon flux is $\sim 3 \times 10^{11}$ photons s^{-1} at the W L_3 edge at a beam current of 200 mA. The energy resolution is ~ 0.8 eV FWHM (full width at half maximum for Si (220)). Further details on the beamline can be found in Proux et al. (2005, 2006).

All measurements were performed at the W L_3 edge (10.207 keV). The energy calibration of monochromators was performed using the first maximum of the derivative of a spectrum of a $4 \mu\text{m}$ thick tungsten metal foil (10.207 keV). At P65 (PETRA III), in situ spectra were measured using a beam size of $0.5 \text{ mm} \cdot 0.5 \text{ mm}$ ($h \cdot v$) with continuous scan mode and a maximum scan range from 10.050 to 11.207 keV. All measurements at P65 were made in transmission mode, i.e., measuring intensities of the incident (I_0) and transmitted (I_1) X-ray beam. At BM30 (ESRF), the beam size was $210 \mu\text{m} \cdot 170 \mu\text{m}$ ($h \cdot v$, FWHM) at 10.5 keV. Here, in situ XAFS spectra were collected in transmission and fluorescence mode using step-scan mode and a maximal scan range from 10.090 to 11.060 keV. Fluorescence spectra were recorded using a 30-element Ge detector (Canberra Packard Central Europe GmbH).

2.4 Dissolution experiments

Dissolution experiments were performed at P65 (PETRA III, DESY). Here, all samples consisted of a small piece of solid material, either CaWO_4 , WO_3 , or $\text{WO}_{2.7}$, and an aqueous fluid of variable composition (details are given in Table 1). Each experiment was started by aligning the autoclave on the horizontal and vertical axes to ensure an optimal measurement position; i.e., the X-ray beam focused on only the fluid. After collecting a spectrum at room temperature, temperature was increased to the first experimental run temperature (T_{exp}), usually at 100°C , and consecutive spectra were collected until a steady state was reached; i.e., no further changes in the amplitude of the edge jump were observed for at least 10 spectra. The concentrations of W in the fluid were calculated from the amplitude of the edge jump ($e\text{H} = \Delta\mu l$, with $\Delta\mu$ being the change in the linear absorption coefficient and l the thickness of the sample) under steady-state conditions using

$$m_{\text{W}} = \frac{e\text{H}}{\Delta\sigma_{\text{W}} l M_{\text{W}} d_{\text{fluid}}}, \quad (1)$$

where, for any given P and T , m_{W} is the molal W aqueous concentration (mol kg^{-1} of solution), $\Delta\sigma_{\text{W}}$ is the change in

Table 1. Summary of starting materials and pressure and temperature conditions and an estimation of W solubility from solubility experiments.

Starting material	P [MPa]	W concentration in the fluid [$\times 10^{-4}$ mol kg^{-1}]						
		100 °C	150 °C	200 °C	250 °C	300 °C	350 °C	400 °C
Solid	Aqueous fluid*							
CaWO_4	H_2O	40	0.68 (± 0.32)		0.26 (± 0.08)			
CaWO_4	H_2O	50	0.33 (± 0.26)		0.23 (± 0.19)			
CaWO_4	1 m NaCl	40	8.6 (± 0.6)		11 (± 0.8)		8.2 (± 1.3)	6.3 (± 1.6)
$\text{WO}_{2.7}$	H_2O	40			3.9 (± 0.7)		4.7 (± 1.1)	
$\text{WO}_{2.7}$	H_2O	50	1.9 (± 0.4)	2.0 (± 0.5)	2.5 (± 0.6)	2.7 (± 1.0)	5.3 (± 0.7)	
$\text{WO}_{2.7}$	2 m NaCl	40	3.8 (± 0.4)		5.5 (± 0.4)		22 (± 6)	17 (± 2)
$\text{WO}_{2.7}$	2 m NaCl + qtz	40	5.2 (± 0.9)		11 (± 0.9)		18 (± 2)	
$\text{WO}_{2.7}$	2 m NaCl + 1 m HCl	40			2.8 (± 0.7)		9.0 (± 3)	19 (± 1)
$\text{WO}_{2.7}$	1 m HCl	40	1.8 (± 0.2)		2.6 (± 0.9)		7.3 (± 0.8)	11 (± 1)
WO_3	H_2O	40	4.0 (± 2.6)		8.1 (± 2.3)		24 (± 2)	
WO_3	H_2O	50	0.63 (± 0.39)	1.2 (± 0.5)	2.8 (± 0.9)	4.0 (± 0.8)	5.3 (± 1.5)	
WO_3	2 m NaCl	50	1.2 (± 0.5)		6.8 (± 0.1)		20 (± 2)	
WO_3	1 m HCl	40	1.7 (± 0.6)		1.8 (± 0.4)		4.5 (± 1.2)	11 (± 2)
								4.1 (± 2.7)

* m – mol kg^{-1} H_2O ; qtz – addition of SiO_2 in experiment; analytical errors are reported within 1 SD.

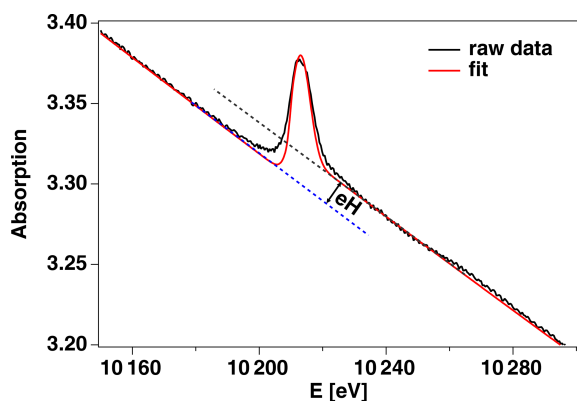


Figure 1. Fit procedure applied to the raw data to determine the amplitude of the edge jump exemplary for a single spectrum of an experiment at 300 °C and 500 bar ($\text{WO}_3 + 2\text{ m NaCl}$). The precision of fit depends on the signal-to-noise ratio and amplitude of the edge jump.

the total absorption cross-section of W over the W L_3 edge ($\text{cm}^2\text{ g}^{-1}$), l is the optical path length inside the cell (cm), M_{W} is the atomic weight of W ($0.18384\text{ kg mol}^{-1}$) and d is the density of the fluid (g cm^{-3}) (e.g., Pokrovski et al., 2005). This procedure was repeated at various temperature steps up to a maximum of 400 °C. The amplitude of the edge jump (eH) was extracted from each experimental spectrum using a fitting routine that combines a polynomial function for background removal, an error function to determine eH, and a Gaussian function to determine the peak location and width of the white line. An example of the fitting procedure applied is shown in Fig. 1. At the end of an experiment, the residual solid was recovered and characterized with XRD. Before and after the runs, glassy carbon cells were rinsed and boiled in aqua regia to avoid cross-contamination between runs. The quantification procedure has been intensively tested by various authors in the past (e.g., Pokrovski et al., 2005; Testemale et al., 2009) and determined to be accurate within 5 % or better. Here, the nominal concentrations of the solutions used for EXAFS analysis were verified to within 10 %, which we consider an estimate of the maximum uncertainty.

2.5 In situ measurements of W speciation with EXAFS and data treatment

During dissolution experiments at P65 (PETRA III), summed spectra were used to assess the speciation of W in H_2O , NaCl and HCl solutions. Yet the different number of spectra to be summed resulted in a variable and often low signal-to-noise ratio, and only the XANES region is therefore interpretable. To gain further information on the local structure of W, in situ EXAFS data were collected on 0.03 m W in H_2O (from this point, m is $\text{mol kg}^{-1}\text{ H}_2\text{O}$) and 0.01 M NaOH, as well as on 0.05 m in 0.1 M HCl solutions that were not in equilibrium with a solid phase, up to 300 °C and 50 MPa

(P65) or 60 MPa (BM30). These W-bearing solutions were produced by dissolving sodium tungstate ($\text{Na}_2\text{WO}_4 \cdot 2\text{H}_2\text{O}$) in H_2O , NaOH and HCl. The data reduction procedure included the xafsX software package (Winterer, 2022, and references therein), which was used to extract the EXAFS signal from the measured absorption spectra. A polynomial fit was used to remove the background in the energy region below the edge, the edge position E_0 was determined using the inflection point of an error function that was fitted together with a Gaussian function to the edge, and the step height of the error function was used for normalization. The background of the EXAFS was determined using a cubic spline function minimizing the signal $< 1\text{ \AA}$ in the Fourier transform. A Kaiser–Bessel filter was applied to Fourier-transform (FT) the k^3 -weighted EXAFS oscillations ($\chi(k)$). The EXAFS data were fitted using the xafsX software (Winterer, 2022) to derive structural information on W complexation (first shell only). The choice of fit model depends on the pH of the solution due to its strong impact on the local structure. For H_2O and more basic solutions, we employed the standard fit procedure, which is based on a symmetric Gaussian pair correlation. Under acidic conditions and temperature $\leq 100\text{ °C}$, strong configurational disorder in the W–O coordination shell made it necessary to split the fit into three contributions with different W–O distances, which is consistent with Hoffmann et al. (2000). One spectrum could be best described using an asymmetric pair correlation based on a weighted sum of exponentials provided by xafsX (Winterer, 2022). This fit includes an additional asymmetry parameter. The theoretical amplitude and phase function were calculated using FEFF 6.0 (e.g., Rehr et al., 2010) with simple molecular models as input structure, similarly to in Hoffmann et al. (2000). Results are in accordance with crystallographic data of crystalline phases such as $\text{Na}_2\text{WO}_4 \cdot \text{H}_2\text{O}$, CaWO_4 and WO_3 , which we used to test the fit procedures. Further, we used FEFF 9.04 (e.g., Rehr et al., 2010) to calculate the XANES spectra of W in tetrahedral and distorted octahedral coordination. These calculations are based on the structure of orthorhombic $\text{Na}_2\text{WO}_4 \cdot 2\text{H}_2\text{O}$ (Farrugia, 2007, ICSD 240882) for the tetrahedral symmetry and that of triclinic WO_3 (Diehl et al., 1978, ICSD 1620) for the distorted octahedral symmetry. First the self-consistent-field optimization of the potentials was performed using a cutoff of 5 \AA . Then the spectra of only the first coordination shell were calculated. In the case of WO_3 , an average of all four W sites was computed. The energy scale was shifted to match the experimental spectra.

2.6 Thermodynamic modeling of tungsten solubility under hydrothermal conditions: data sources and models

The Haar–Gallagher–Kell and Marshall and Franck models (Marshall and Franck, 1981; Kestin et al., 1984) were used to determine the thermodynamic properties and dissoci-

ation constant of H₂O for our experimental conditions. Those models are implemented in the HCh software that was used in this study (Shvarov, 2008).

Six aqueous tungsten species were used, namely WO₄²⁻, HWO₄⁻, H₂WO₄⁰, H₃WO₄⁺, NaWO₄⁻ and NaHWO₄⁰. All of these species have already been used for the thermodynamic description of W solubility in aqueous fluids (Ivanova and Khodakovskiy, 1968; Rafal'sky et al., 1984; Wesolowski et al., 1984; Heinrich, 1990; Gibert et al., 1992; Shock et al., 1997; Wood and Samson, 2000; Minubaeva, 2007; Wang et al., 2019). The thermodynamic properties for WO₄²⁻ species described on the basis of Helgeson–Kirkham–Flowers (HKF) model (Helgeson et al., 1981; Tanger and Helgeson, 1988) were adopted from Shock et al. (1997) without any changes. The thermodynamic properties for HWO₄⁻, H₃WO₄⁺ and NaWO₄⁻ species were optimized using our solubility experiments (Table S1 in the Supplement); the H₂WO₄⁰ species was optimized using data in standard conditions (Table S3) and the hydrothermal experiments of Wood and Vlassopoulos (1989); and the NaHWO₄⁰ species was described as an analogue of KHSO₄⁰ species taken from Sverjensky et al. (1997) (for more details, see below). In addition to the six aqueous tungsten species mentioned, the following aqueous species were considered system components in the thermodynamic modeling: H⁺, OH⁻, Na⁺, Cl⁻, NaOH⁰, NaCl⁰, HCl⁰, CO₃²⁻, HCO₃⁻, H₂CO₃⁰, NaCO₃⁻, NaHCO₃⁰, SiO₂⁰, Si₂O₄⁰, C₂H₆⁰, HCOOH⁰, HCOO⁻, CH₃COOH⁰, CH₃COO⁻, C₂O₄²⁻, HC₂O₄⁻, H₂C₂O₄⁰, NaCH₃COO⁰, Na(CH₃COO)₂⁰, O₂⁰, H₂⁰, CO₂⁰, CH₄⁰ and CO⁰. Thermodynamic data for major cations; anions; and their ion pairs, organic species and CO were taken from Johnson et al. (1992), Shock et al. (1997) and Sverjensky et al. (1997). SiO₂ and Si₂O₄ aqueous species were adopted from Sverjensky et al. (2014). Aqueous non-electrolytes O₂, H₂, CO₂ and CH₄ were taken from Akin'fiev and Diamond (2003). HCl⁰ (aq) species were taken from Tagirov et al. (1997). Values for the extended parameter of the Debye–Hückel equation for NaCl were taken from Oelkers and Helgeson (1991). For the calculations of scheelite and ferberite solubilities, iron and calcium aqueous species were added to the system. Iron aqueous species, including Fe²⁺, FeOH⁺, FeO⁰, HFeO₂⁻, Fe³⁺, FeOH⁺⁺, FeO⁺, HFeO₂⁰ and FeO₂⁻, were taken from Shock et al. (1997), whereas FeCl⁺, FeCl₂⁰ and FeCl₄²⁻ were taken from Sverjensky et al. (1997) and Testemale et al. (2009), respectively. Calcium aqueous species, including Ca²⁺, CaOH⁺, CaCl₂ and CaCl⁺, were adopted from Johnson et al. (1992). Thermodynamic data for tungsten oxides WO₃ (cryst), WO_{2.7} (cryst), scheelite, quartz, graphite and ferberite solid phases were taken from Han et al. (2020), Barin (1995), Barin and Knacke (1973), Robie and Hemingway (1995), and Zhidikova and Khodakovskiy (1984) (Table S2).

The activity coefficient of each ionic species was calculated using the extended Debye–Hückel equation (Helgeson

et al., 1981; Oelkers and Helgeson, 1990, 1991):

$$\log \gamma_i = -\frac{A \cdot [z_i]^2 \cdot \sqrt{I}}{1 + B \cdot a^\circ \cdot \sqrt{I}} + b_\gamma \cdot I + \Gamma, \quad (2)$$

in which *A* and *B* are constants representing Debye–Hückel law parameters; *b_γ* is the extended parameter for NaCl from Helgeson and Kirkham (1974); *a^o* is the distance of the closest approach which is specific to the ion of interest; *z* is the charge of the ion; *Γ* is a molarity-to-molality conversion factor; and *I* is the ionic strength calculated with

$$I = \frac{1}{2} \sum_{i=1}^n c_i z_i^2, \quad (3)$$

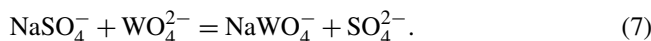
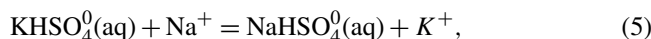
where *c_i* is the molar concentration of ion *i* (mol L⁻¹) and *z_i* is the charge of that ion. Parameter *I* is the true ionic strength of solution. The activity coefficients of neutral species were assumed to be unity.

The formation constants of aqueous tungsten species WO₄²⁻, HWO₄⁻, H₂WO₄⁰, H₃WO₄⁺, NaWO₄⁻ and NaHWO₄⁰ at different temperatures were fitted to the Bryzgalin–Ryzhenko model (Ryzhenko et al., 1985; Bryzgalin and Rafal'sky, 1982) modified by Shvarov and Bastrakov (1999):

$$pK_{T,P} = pK_{298K, 1 \text{ bar}} \times 298.15/T + f(T, P) \times (zz/a)_{\text{eff}}, \quad (4)$$

where *K* is the dissociation constant of the ion pair; *pK* = -log₁₀*K*; *pK*_{298K, 1 bar} is the *pK* of reaction under standard conditions; *T* is temperature in kelvins; *P* is pressure in bars; *f(T, P)* is a species-independent function computed from the dissociation constant of water as a function of *T* and *P* (Marshall and Franck, 1981); and (zz/*a*)_{eff} is a property of a complex, where (zz/*a*)_{eff} = *A*_(zz/a) + *B*_(zz/a)/*T* (*T* in kelvins), with *A*_(zz/a) and *B*_(zz/a) being *T*-independent constants for each complex, i.e., the fitting parameters.

The formation constants of alkali-tungstate ion pairs NaWO₄⁻ and NaHWO₄⁰ (aq) were assumed to be equal to those of NaSO₄⁻ and KHSO₄⁰, respectively, for which adequate sets of HKF parameters are available (Pokrovski et al., 1995; Sverjensky et al., 1997). This assumption translates into *K_{T,P}* = 1 for the following isocoulombic ion exchange reactions at all temperatures and pressures:



The thermodynamic properties of tungsten species obtained in this study are reported in Tables 4, S1 and S3–S6 of the Supplement and are discussed in Sect. 4.3 and 4.4.

3 Experimental results

All data provided in Figs. 2 to 11 and Table 3 are available in an online data repository and can be downloaded under <https://doi.org/10.5880/figgeo.d.2024.002> (Borchert et al., 2024).

Table 2. Summary of fluid composition, pressure and temperature conditions, and density used for calculation of W concentration. Densities of H₂O are taken from the NIST Chemistry WebBook (Lemmon et al., 2019). For all other solutions, fluid chemistry is recalculated to NaCleq. and corresponding densities are determined using SoWat, i.e., the Sodium chloride–Water model by Driesner and Heinrich (2007) and Driesner (2007).

Aqueous fluid	<i>P</i> [MPa]	Density of solution [g cm ⁻³]						
		100 °C	150 °C	200 °C	250 °C	300 °C	350 °C	400 °C
H ₂ O	40	0.976		0.891		0.764		
H ₂ O	50	0.980	0.943	0.897	0.842	0.777		
1 <i>m</i> NaCl	40	1.013		0.932		0.818	0.740	
2 <i>m</i> NaCl (± qtz)	40	1.047		0.967		0.863	0.799	
2 <i>m</i> NaCl + 1 <i>m</i> HCl	40			0.991		0.885	0.822	0.736
2 <i>m</i> NaCl	50	1.051		0.975		0.873		
1 <i>m</i> HCl	40	1.004		0.920		0.812	0.695	0.606

Table 3. Summary of EXAFS analysis for the first coordination shell, describing the W–O pair distribution. The number of oxygen neighbors *N* was fixed to given value. *R* denotes the W–O distance, Sigma² the variance of *R*, and Δ*E*₀ the shift of *E*₀. Except for the run at 200 °C, all W–O parameters listed were determined assuming a Gaussian distribution of the W–O pair distribution. The large static disorder of the octahedral coordination in HCl solution at 20 and 100 °C was described using three W–O paths. At 200 °C a fit based on a single but asymmetric pair distribution was used. Data at 300 °C in HCl solution and in H₂O could be described with a single W–O path. pH values were calculated using the HCh software package (Shvarov, 2008).

Temperature	<i>N</i>	<i>R</i> [Å]	Sigma ² [Å ²]	1 Δ <i>E</i> ₀ [eV]	Asymmetry
Solution: 0.03 <i>m</i> Na ₂ WO ₄ · 2 H ₂ O in H ₂ O, 60 MPa pH _{25 °C} = 8.92					
20 °C	4	1.774 ± 0.005	(0.19 ± 0.01) × 10 ⁻²	15.7 ± 0.1	n/a
300 °C	4	1.771 ± 0.005	(0.20 ± 0.01) × 10 ⁻²	15.0 ± 0.1	n/a
Solution: 0.05 <i>m</i> Na ₂ WO ₄ · 2 H ₂ O in 0.1 <i>m</i> HCl, 50 MPa, pH _{25 °C} = 4.55					
20 °C	2	1.730 ± 0.006	(0.30 ± 0.01) × 10 ⁻²	9.1 ± 0.1	n/a
	2	1.90 ± 0.01	(0.35 ± 0.01) × 10 ⁻²		n/a
	2	2.233 ± 0.006	(1.5 ± 0.01) × 10 ⁻²		n/a
100 °C	2	1.738 ± 0.006	(0.39 ± 0.01) × 10 ⁻²	8.4 ± 0.1	n/a
	2	1.90 ± 0.01	(0.36 ± 0.01) × 10 ⁻²		n/a
	2	2.278 ± 0.006	(3.10 ± 0.01) × 10 ⁻²		n/a
200 °C	6	1.94 ± 0.01	(0.08 ± 0.05) × 10 ⁻²	12.5 ± 0.1	0.11 ± 0.01
300 °C	4	1.775 ± 0.01	(0.98 ± 0.80) × 10 ⁻²	11.6 ± 0.1	n/a

n/a: not applicable.

3.1 Solubility experiments

An example of the W concentration in the fluid monitored as a function of runtime elapsed after reaching *T*_{exp} is presented in Fig. 2, where WO₃ coexists with various aqueous fluids at different run temperatures. A summary of all determined W concentrations is depicted in Figs. 3 and 4, as well as in Table 1 as a function of starting materials, fluid composition, pressure and temperature. Fluid densities used for the determination of concentrations are given in Table 2. The attainment of equilibration between solids and solution was tested with a few long-runtime experiments at 100 °C, e.g., as shown for the H₂O solution (Fig. 2). The data of this run indicate that a steady state was reached after 3 to 4 h, showing

only non-systematic fluctuations at longer durations. Please note that error bars of the single measurements in Fig. 2 are based on the error of the fit and are typically smaller than the symbols. Moreover, after 1 h runtime, the concentration of W in the fluid did not differ significantly to the one after 10 h of runtime. Therefore, all other experiments were run for at least 1 h and were terminated when no further significant increase in the observed W concentration was detected. Equilibration in HCl solutions is significantly faster, as the time series had already approached a quasi-constant value after ca. 1 h. Only the equilibration at 200 °C in 2 *m* NaCl solution does not seem to be in a steady state, although the runs at 100 and 300 °C both show constant values after 1 h. The rea-

Table 4. Bryzgalin–Ryzhenko (BR) model parameters derived for tungsten species based on the formation constants determined in this study.

Reaction	$pK_{298\text{K}}$	$A_{(zz/a)}$	$B_{(zz/a)}$	Source
$\text{NaWO}_4^- = \text{Na}^+ + \text{WO}_4^-$	4.400 ^e	0.622	0	This study ^a
$\text{H}_2\text{WO}_4^0 = 2\text{H}^+ + \text{WO}_4^-$	8.140	1.608	0	This study ^b
$\text{HWO}_4^- = \text{H}^+ + \text{WO}_4^-$	4.737	1.100	0	This study ^c
$\text{H}_3\text{WO}_4^+ = 3\text{H}^+ + \text{WO}_4^-$	10.986 ^e	1.496	0	This study ^d

^a Optimized from solubility experiments with $\text{WO}_{2.7}$ (cr) (\pm quartz) in 2 m NaCl at 100–300 °C and 400 bar (this study). ^b Thermodynamic properties of H_2WO_4^0 (aq) species were derived from hydrothermal experiments of Wood and Vlassopoulos (1989), whereas the $pK_{298\text{K}}$ values were taken from Table S3 and averaged. ^c Optimized from solubility experiments with WO_3 (cr) in pure H_2O at 150–300 °C and 500 bar. The $pK_{298\text{K}}$ for HWO_4^- optimized in this study is consistent with the $pK_{298\text{K}}$ reported by Perrin (1969) (Table S3). ^d Optimized from solubility experiments with $\text{WO}_{2.7}$ (cr)/ WO_3 (cr) in 1 m HCl (this study). ^e The $pK_{298\text{K}}$ values for H_3WO_4^+ and NaWO_4^- species were optimized from hydrothermal experiments and should be taken with caution.

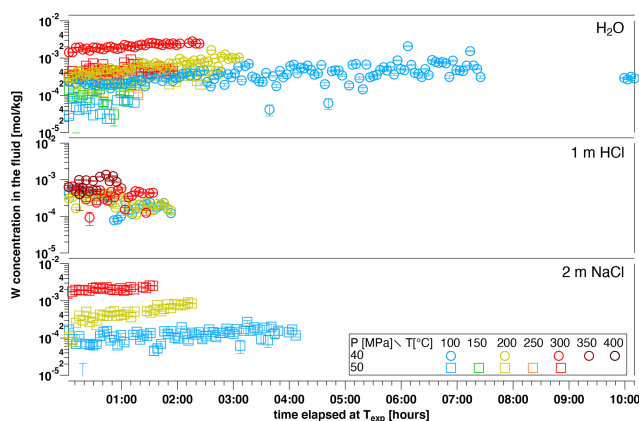


Figure 2. W concentration in various aqueous fluids coexisting with a piece of WO_3 as a function of time elapsed since reaching the indicated experimental temperature. For each experiment and each experimental temperature, scans were recorded for at least 1 h (an exception is the 400 °C run in WO_3 + 1 m HCl; this experiment was aborted earlier due to a fluid leakage).

son for this is unclear. Overall, the time series indicate that the determined concentrations should be close to equilibrium values.

The final W concentrations (Table 3) were determined from the average concentration of measurements after equilibration was attained, and the errors are based on the standard deviation of the averaged values. Thus, the error includes the fluctuations over time represented in Fig. 2. The majority of dissolution experiments were performed using either WO_3 or $\text{WO}_{2.7}$ as the solid starting material. Scheelite decomposes in HCl and precipitates W-oxides, producing unreliable W concentrations in such runs (cf. Xiao et al., 2022). Both WO_3 and $\text{WO}_{2.7}$ have been identified as run products during scheelite dissolution experiments in HCl-bearing solutions, with no clear preference as determined by micro-XRD and Raman spectroscopy on the recovered grains. In runs with $\text{WO}_{2.7}$ or WO_3 as the starting material, no conversion of the re-

spective starting oxides could be detected as the solids were characterized after runs by micro-XRD. The maximum W concentration observed for WO_3 and $\text{WO}_{2.7}$ dissolution is around $2 \times 10^{-3} \text{ mol kg}^{-1}$ at $T \geq 300 \text{ °C}$ in 2 m NaCl solutions (Fig. 3). The data show an overall increase in W concentrations with increasing temperature up to $\sim 300 \text{ °C}$ for almost all fluid compositions studied. For WO_3 , two runs were performed in pure water, at 50 and 40 MPa, respectively. Surprisingly, the run at 40 MPa results in concentrations that are up to 1 order of magnitude higher than those at 50 MPa. The reason for this discrepancy is unclear, and the results can only be explained by contamination of the glassy carbon cell that was used in this particular run. Despite this unexplained deviation from expected behavior, the temperature dependence of the H_2O run at 40 MPa is similar to all other runs. Ignoring this run of WO_3 in H_2O and HCl solutions for both oxide compounds. There seems to be no significant effect of the starting oxide, i.e., $\text{WO}_{2.7}$ or WO_3 , on the W concentration in the fluid. The highest W concentrations were observed in NaCl-bearing solutions, and these were not significantly affected by the inclusion of quartz as an additional solid phase.

In HCl-free solutions, scheelite is a stable phase and several runs were performed to compare W concentration in fluids that were equilibrated with this mineral phase (Fig. 4). W concentrations in H_2O are lower by about 1 order of magnitude compared to the W-oxides, with almost no temperature dependence, as shown in Fig. 4. In 1 m NaCl solution, W contents are on the order of $10^{-3} \text{ mol kg}^{-1}$ and show no significant dependence on temperature up to 350 °C.

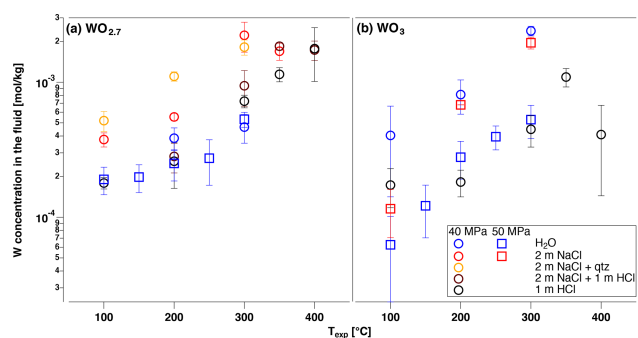


Figure 3. Average W concentration determined from the amplitude of the edge jump for aqueous fluid compositions with experimental conditions indicated and the two solid materials: (a) $\text{WO}_{2.7}$ and (b) WO_3 .

3.2 W speciation in high- P - T fluids by EXAFS and XANES spectroscopy

W speciation was studied in a suite of fluids that were produced by dissolution of $\text{Na}_2\text{WO}_4 \cdot 2\text{H}_2\text{O}$ (s) in H_2O , 0.01 M NaOH and 0.1 m HCl at pressures of 50 and 60 MPa and up to 300 °C. The aqueous solution has an alkaline pH under ambient conditions at ca. 8.9, whereas the HCl solution is at ca. pH 4.6 under ambient conditions (pH values were calculated). The spectra taken on the NaOH solution were identical to those in H_2O and thus are not further discussed.

EXAFS spectra and the analysis of the H_2O solution are presented in Fig. 5a–d. The EXAFS and Fourier transform (FT) of the H_2O solution indicate that there is only one contribution to the EXAFS signal, stemming from the oxygen neighbors. A fit of the data with N fixed to four oxygens reveals an average distance of 1.774 Å at 20 and 300 °C (cf. Table 3, Fig. 5d). This distance is typical of W in tetrahedral coordination, e.g., as found in scheelite or crystalline $\text{Na}_2\text{WO}_4 \cdot 2\text{H}_2\text{O}$ (Zalkin and Templeton, 1964; Farugia, 2007). Inspection of the residual (Fig. 5b) indicates a significant residual amplitude with a strong edge-like signal at ca. 8.2 \AA^{-1} . This feature can be assigned to a multi-electronic KN_5 excitation (260.5 eV; Fuggle and Mårtensson, 1980) using the $Z+1$ model (Li et al., 1992). As the position of this feature is in phase with the EXAFS signal, it cannot be removed by the data reduction procedure and thus adds artificial amplitude to the EXAFS. Also fitting the N parameter would yield more than five O neighbors, which is physically unfeasible at the fitted W–O distance.

EXAFS spectra of the HCl solution and their analysis are presented in Fig. 6a–d. The EXAFS and Fourier transform indicate that there are two contributions to the EXAFS signal from two coordination shells up to 200 °C and only one at 300 °C. Further, the overall amplitude is considerably smaller than that of the H_2O solution and the first maximum of the FT shows splitting, both of which indicate strong static dis-

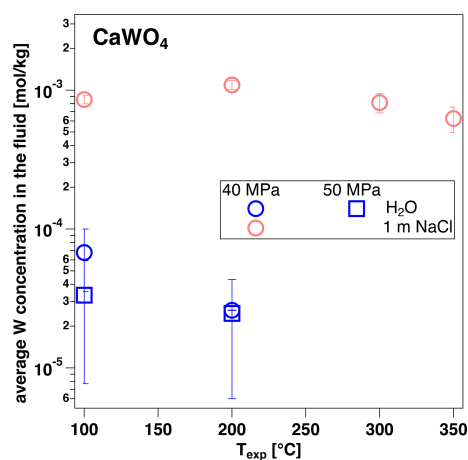


Figure 4. Average W concentration determined from the amplitude of the edge jump for aqueous fluid compositions with experimental conditions indicated and the solid material CaWO_4 (synthetic scheelite).

order in the W–O coordination shell. The second maximum of the FT at ca. 3.2 Å can be assigned to W–W distance, as reported earlier for acidic W solutions (Hoffmann et al., 2000). A fit of the Fourier-filtered signal of the first shell reveals a strongly distorted octahedral coordination at 20 and 100 °C, with three pairs of W–O distances at 1.730, 1.90 and 2.33 Å (cf. Table 3, Fig. 6d). This structural model was developed using a spectrum of triclinic crystalline WO_3 , which shows a similar coordination and distribution of W–O distances (Diehl et al., 1978). At 200 °C the disorder seems to decrease and the data can be described with a single but still asymmetric W–O pair distribution, with six neighbors and an average distance of 1.94 Å. At 300 °C, a symmetric pair distribution with only four neighbors and 1.775 Å, similar to the value of the H_2O solution, is fitted.

The XANES spectra for the two solutions measured at 20 and 300 °C are shown in Fig. 7. At 20 °C the two solutions differ (i) in the width of the main crest at the edge, which is broadened for the HCl solution; (ii) in the intensity of the feature at ca. 10 225 eV, which is lower for the HCl solution; and (iii) in the position of the first EXAFS oscillation, i.e., ca. 10 270 eV for the HCl solution and ca. 10 280 eV for H_2O . Particularly the latter is sensitive to the average W–O distance (Bianconi et al., 1983; Wilke et al., 2007), and a position at lower energies is directly related to longer average W–O distance. The differences in the spectra are confirmed by calculated spectra that are based on W–O polyhedra found in crystalline WO_3 (distorted octahedral) and $\text{Na}_2\text{WO}_4 \cdot 2\text{H}_2\text{O}$ (tetrahedral). These spectra confirm the relative differences observed in the experimental ones of the two solutions at 20 °C, even though the calculation does not replicate the absolute intensity of the peak at the edge. At 300 °C, the spectrum of the H_2O solution virtually does not change, whereas the one of the HCl solution shows signifi-

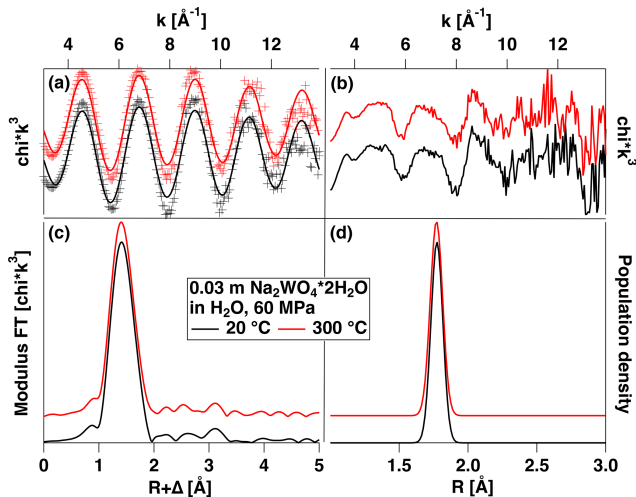


Figure 5. (a) Experimental k^3 -weighted EXAFS and fit of a solution of $\text{Na}_2\text{WO}_4 \cdot 2\text{H}_2\text{O}$ dissolved in H_2O measured under the conditions indicated. (b) Residual of fits of (a). (c) Modulus of Fourier transform of the EXAFS shown in (a). (d) W–O pair distributions resulting from the fit and corresponding to the fitted parameters shown in Table 3. See text for further discussion.

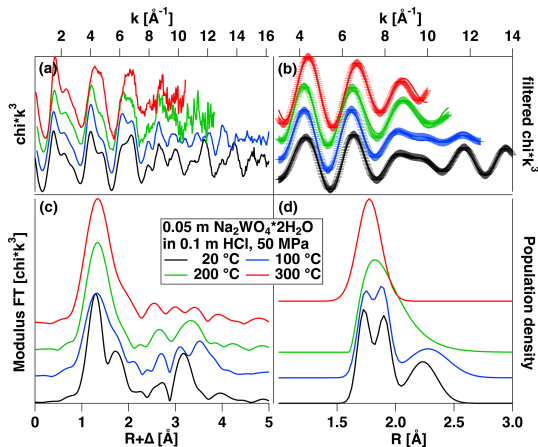


Figure 6. (a) Experimental k^3 -weighted EXAFS of a solution of $\text{Na}_2\text{WO}_4 \cdot 2\text{H}_2\text{O}$ dissolved in 0.1 m HCl measured under the conditions indicated. (b) Fourier-filtered EXAFS signal of the first coordination shell (range 0.8–2.2 \AA) in (a) and fit. (c) Modulus of Fourier transform of the EXAFS shown in (a). (d) W–O pair distributions resulting from the fit and corresponding to the fitted parameters shown in Table 3. See text for further discussion.

cant differences from the one at 20 °C, i.e., narrowing of the maximum at the main crest, higher intensity at 10 225 eV and a much broader first EXAFS oscillation that shows stronger intensity at 10 280 eV than at 20 °C. Overall, the XANES becomes more similar to that of the H_2O solution.

Because of the rather low W contents reached in the dissolution experiments ($\leq 10^{-3}$ mol kg^{-1}), the total acquisition time was only sufficient to collect XANES spectra, which are presented in Fig. 8 for runs at 300 °C with $\text{WO}_{2.7}$ used

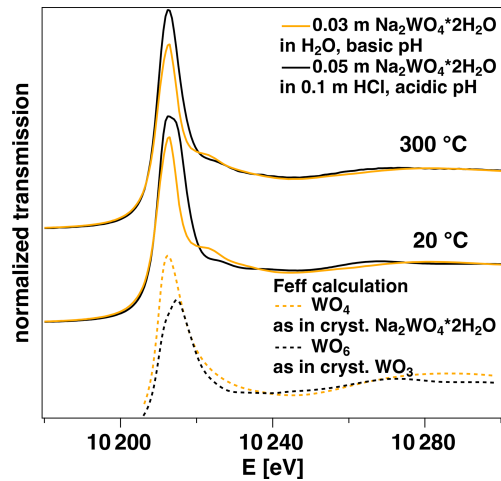


Figure 7. XANES spectra of the solutions shown in Figs. 5 and 6 under the conditions indicated. The experimental spectra are compared to theoretical spectra computed using FEFF for a WO_4 coordination shell in tetrahedral symmetry as found in crystalline $\text{Na}_2\text{WO}_4 \cdot 2\text{H}_2\text{O}$ and a WO_6 coordination shell in distorted octahedral symmetry as found in crystalline WO_3 .

as a solid. Only the run with H_2O and two runs with NaCl solution provide spectra that show a signal-to-noise ratio that allows us to estimate the W speciation. In the spectra of the NaCl solution, the position of the first EXAFS oscillation is at ca. 10 280 eV and the peak of the main edge is slightly broadened. The spectrum of the H_2O run is worse in quality. We can still show that the spectra of the run with H_2O did not significantly change during equilibration and acquisition over 10 h by comparing the average of the first 10 spectra and of the complete series (Fig. 8). A direct superimposition with those of the NaCl solutions indicates that the position of the EXAFS maximum seems to be shifted to higher energy for the H_2O experiment, indicating a shorter W–O bond length than for the NaCl solutions. All other spectra do not allow for any significant assignment.

4 Discussion

4.1 Tungsten solubility

The W concentrations in fluids determined in this study can be compared to both previous experiments (Wang et al., 2019; Wood, 1992; Wood and Vlassopoulos, 1989) and natural W contents in fluid inclusions from different ore deposits. In our experiments, W concentrations in the fluid range between 6×10^{-5} and $\sim 2 \times 10^{-3}$ mol W kg^{-1} (i.e., up to ~ 400 $\mu\text{g g}^{-1}$) with the maximum at 300–350 °C. This is significantly higher than reported in previous experiments. For instance, Wang et al. (2019) report a similar increase in WO_3 solubility with NaCl content of the solution, albeit with a maximum concentration of $\sim 6 \times 10^{-4}$ mol kg^{-1} H_2O at 350 °C and vapor-saturated water pressure for an aqueous

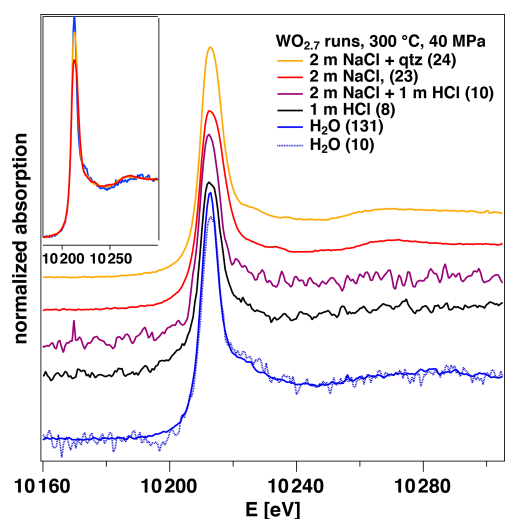


Figure 8. Comparison of W XANES spectra of different fluids collected in experiments using $\text{WO}_{2.7}$ as a solid material at 300 °C and 40 MPa. The number given in parentheses refers to the number of averaged single spectra for each experiment. The inset shows a superimposition of the two spectra of the NaCl solution on the one of H_2O run.

solution containing 1.4 m NaCl (pH 3.7). In comparison, we report W concentrations up to $2 \times 10^{-3} \text{ mol kg}^{-1}$ for similar T and X_{NaCl} values. Comparison to earlier experiments by Wood (1992) and Wood and Vlassopoulos (1989) is more difficult as they reported potential issues with fluid sampling as the reason for large discrepancies in their dataset. We however note that W concentrations reported for experiments at 400 °C and 100 MPa using 0.49 m HCl ($\sim 7 \times 10^{-4} \text{ mol kg}^{-1} \text{ H}_2\text{O}$) are very similar to our results at 40 MPa using 1 m HCl, e.g., $\sim 4.7 \times 10^{-4}$ to $7.3 \times 10^{-4} \text{ mol kg}^{-1} \text{ H}_2\text{O}$ at 300 °C and $\sim 1 \times 10^{-3} \text{ mol kg}^{-1} \text{ H}_2\text{O}$ at 350 °C. Similarly, the W concentrations reported in 1–6 m NaCl solution at 500 °C and 100 MPa (8×10^{-3} to $1.4 \times 10^{-2} \text{ mol kg}^{-1} \text{ H}_2\text{O}$) are in line with those reported here at lower temperatures ($2 \times 10^{-3} \text{ mol kg}^{-1} \text{ H}_2\text{O}$ for 2 m NaCl at $T > 300$ °C).

4.2 Speciation of tungsten in the fluids by EXAFS and XANES

In order to constrain the W species in the fluid and to be able to interpret XANES spectra obtained during dissolution experiments, we present a few measurements of solutions derived from dissolving $\text{Na}_2\text{WO}_4 \cdot 2\text{H}_2\text{O}$ in H_2O or 0.1 m HCl solution. Dissolution of this compound in water leads to pH 8.5 under ambient conditions, so this spectrum represents the species in alkaline fluids, which corresponds to the tetrahedral WO_4^{2-} species (Hoffmann et al., 2000; Dewan and Kepert, 1973) and shows no further contributions by higher-coordination shells. Further addition of NaOH does not change the spectrum (not shown). The W–O distance of 1.77 Å determined for H_2O and NaOH so-

lutions is consistent with tetrahedral coordination. Further, there is no change in this coordination for temperatures up to 300 °C, which is in agreement with the results of Hoffmann et al. (2000) and Mei et al. (2024). We therefore consider this to be the stable monomeric W species under alkaline conditions. Rapid conversion of the tetrahedral species to polytungstate ions by acidification was reported, for example, by Dewan and Kepert (1973), and the change in the EXAFS spectrum from pH 8.5 down to pH 1.9 was documented by Hoffmann et al. (2000). As outlined by those authors and found here as well, not only is this a polymerization reaction of the tungstate ion. It also results in a completely different symmetry for the first shell W–O coordination, which changes to strongly distorted octahedral symmetry. The high static disorder with five to six different W–O distances leads to destructive interference in the EXAFS signal and, thus, to a severe drop in the overall EXAFS amplitude. According to Hoffmann et al. (2000), the pH-dependent conversion to the octahedral W species is already attained at a pH of 7.1 at ambient temperature. At lower pH, longer polymers are formed (Dewan and Kepert, 1973). The spectrum presented here for 0.1 m HCl solution clearly documents the low-amplitude signal of the distorted W complex together with a strong signal by the higher-coordination shell that can be assigned to W–W correlations (cf. Fig. 6d). The signal of the first coordination shell can be described with three pairs of oxygen with distances of 1.73, 1.90 and 2.233 Å, respectively (Table 3), mimicking a broad and asymmetric pair distribution as illustrated in Fig. 6d. In reality, it is very likely that this complex is even composed of six different W–O distances, but such a model outranges the parameters that could confidentially be fitted. The presented fit approach of the first shell was tested on a spectrum of crystalline WO_3 , which shows a distorted W–O octahedral coordination very similar to the one in this fluid at room temperature, as already demonstrated by Hoffmann et al. (2000). The polymerized W species can be traced up to 200 °C by the W–W peak in the Fourier transform at 3–3.5 Å, despite decreasing data quality. At 300 °C, a considerable change in the spectrum is observed, marked by an obvious loss of the contribution by W–W correlations. In addition, the result of the fit, which yields a W–O distance of 1.775 Å, is evidence for a conversion to a mainly tetrahedral W species, although with a larger width of the pair distribution compared to that of the H_2O solution. Mei et al. (2024) studied the coordination of a single tungstate ion in a box of 111 H_2O molecules by ab initio molecular dynamics at 150 °C and higher. They report distorted tetrahedral coordination with two bond lengths of 1.78 and 1.88–1.92 Å, which is not identical to but points towards the distributions found here at temperatures ≥ 200 °C. The difference is due to the fact that polymerization cannot occur if only a single ion is present in the simulation box. Hoffmann et al. (2000) only studied solutions up to 200 °C at 235 bar, and they observed no significant change in the EXAFS with temperature at pH 5.5 and 1.9, consistent with the

observations made in this study. The change in the W species above 200 °C is certainly related to the decrease in the dielectric constant of the solution with increasing temperature, as documented for the pure H₂O system (e.g., Franck et al., 1990). This change in the solvent properties may lead to association of HCl in the fluid and, thus, to conditions favoring the monomeric WO₄²⁻ or other monomeric species. The formation of polymeric tungstate species in hydrothermal fluids was also studied using in situ Raman spectroscopy by Wang et al. (2020a, b) and Carocci et al. (2022) with solutions made by dissolution of potassium (Wang et al.) or sodium (Carocci et al.) tungstate salts. Both groups report the appearance of Raman bands under neutral to acidic conditions that can be assigned to polymeric tungstate species, using the symmetric stretching vibrations of the W=O bonds (ν_1 (W=O)). The stability of the polymeric tungstate species considerably decreases above 200 °C in moderately acidic solutions, and at 300 °C the stability field of the WO₄²⁻ is extended down to pH 6. However, the stability field of polytungstate species in the fluids is significantly enlarged by increased NaCl concentration, acidity or total W content (cf. Wang et al., 2020a, b; Carocci et al., 2022). Our observations made with the HCl solution are consistent with these earlier reports as our experimental run falls into the compositional range in terms of pH and W content, where polymeric tungstate formation is dominant below 200 °C and diminishes at a higher temperature. Furthermore, the calculation in a metastable system for our standard solution of 0.05 m Na₂WO₄ in 0.1 m HCl using thermodynamic properties of polymers reported in Carocci et al. (2022) supports our X-ray absorption spectroscopy (XAS) measurements, giving up to 85 mol %–95 mol % of polymerized W at 100–200 °C and 500 bar and 36 mol % of polymerized W at 300 °C and 500 bar. However, the addition of tungsten oxides to the calculation leads to a decrease in W concentrations to 5×10^{-4} m (100 times) and makes all polymers negligible under thermodynamic equilibrium with tungsten oxides with max concentration 5×10^{-7} m for polymerized W at 100 °C.

The difference in the symmetry of the W–O coordination between the solution of Na₂WO₄ · 2H₂O with H₂O and the one with 0.1 m HCl is also documented by the XANES region of the spectra (Fig. 7). At room temperature, the maximum at the main edge shows a larger width and asymmetry for the HCl solution. There is a clear difference in intensity at ca. 10 225 eV. This feature is more intense and at slightly lower energy for the H₂O solution. Finally, the position of the first EXAFS maximum can be used (ca. 10 280 eV), which is shifted to higher values for the H₂O solution due to the shorter W–O bond length of the tetrahedral W species compared to the distorted octahedral one in the HCl solution. A simple FEFF calculation of a theoretical XANES spectrum for a tetrahedral model and a distorted octahedral model supports the interpretations of the observed spectral differences and the assignment to the differences in coordination. The spectrum of the distorted model shows a larger width and

asymmetry for the maximum at the main edge and lower intensity at 10 225 eV, and the position of the first EXAFS maximum is at lower energy compared to that of the tetrahedral model. Even though the simulated spectra are only based on simple static model structures, they clearly highlight the major differences for the two local arrangements under discussion for the first coordination shell. The spectra recorded at 300 °C for the two solutions become more similar, although not identical. This documents the change in coordination in the case of the HCl solution from a complexation that is dominated by a distorted octahedron towards a state where tetrahedral complexation becomes more dominant. Although the EXAFS analysis points to tetrahedral coordination (see above), the comparison of the two XANES spectra at 300 °C indicates that the conversion is not complete, which would be consistent with the larger width of the fitted W–O pair distribution of the HCl solution from the EXAFS analysis (cf. Figs. 5d and 6d, Table 3).

With this knowledge of the effects of the local structure on the XANES spectra, we can also attempt to assign the dominant coordination from those XANES spectra that were recorded during the dissolution experiments, as shown in Fig. 8. The two spectra taken with near-neutral NaCl solutions provide the best signal-to-noise ratio. All spectral features, particularly the position of the first EXAFS maximum, point towards the distorted octahedral coordination. This interpretation would be in line with the observations made by Carocci et al. (2022) with their NaCl solutions by Raman spectroscopy. Whether polymerization of the W species already plays a role is not discernible from these spectra. Judging by the pH and W-content dependence of the polymerized species presented by Carocci et al. (2022) for 300 °C, it is possible that a mixture of mostly HWO₄⁻ or H₂WO₄⁰ with some W polymers, all with octahedral W–O coordination, is present at least at 300 °C. The spectrum collected for the run where WO_{2.7} was equilibrated with H₂O shows slight but significant difference from those of the NaCl solutions (inset in Fig. 8). Particularly, the difference at the first EXAFS maximum points towards a significant contribution of the tetrahedral WO₄²⁻ species. Again, this interpretation can be supported by the assignment of Carocci et al. (2022), who determined the border between HWO₄⁻/H₂WO₄⁰ and WO₄²⁻ species close to neutral pH at 300 °C, which would also mark the transition from octahedral to tetrahedral species. Unfortunately, the quality of the spectra of the HCl-bearing solutions does not allow any robust assignment for the dissolution experiments presented here. If we apply the systematics of Carocci et al. (2022), we can expect the presence of octahedral HWO₄⁻ or H₂WO₄⁰ species in these solutions, mostly because the W content is too low for the formation of W polymers.

4.3 Thermodynamic modeling of W solubility and W species: optimization of thermodynamic data and evaluation of formation constants

Based on our in situ analysis of W solubility of W-oxides and speciation in high- P - T fluids, we optimized the thermodynamic parameters of the W species (see Sect. 2.6) in the fluid using the HCh code to eventually simulate the solubility of scheelite (CaWO_4) and ferberite, the Fe end-member (FeWO_4) of wolframite.

The dissociation constants of tungstic acid are not well known even at 25 °C, and values reported in the literature vary within 2.5 log units for both steps of dissociation (Table S3; Wood and Samson, 2000; Bychkov and Zuykov, 2005); the same problem also persists under hydrothermal conditions (Table S4; e.g., Heinrich, 1990; Gibert et al., 1992; Wood and Samson, 2000; Wang et al., 2019). Despite the large discrepancies reported for those constants in the literature, the $pK_{298\text{K}}$ values for HWO_4^- and H_2WO_4^0 species were adopted from Perrin (1969). Thermodynamic properties for H_3WO_4^+ , NaWO_4^- and HWO_4^- tungsten species, including their apparent Gibbs free energy of formation and formation constants, were determined from the molality of tungsten, NaCl and HCl in each experiment from this study using the OptimA program (HCh software package; Shvarov, 2008, 2015) (Table S1). Masses corresponding to an excess of the solutes, here WO_3 (cryst) or $\text{WO}_{2.7}$ (cryst) and graphite, were specified in the input file. The thermodynamic properties of H_2WO_4^0 tungsten aqueous species were optimized with OptimA using the experimental data of Wood and Vlassopoulos (1989) and data at ambient conditions from Table S3. The thermodynamic properties of NaHWO_4^0 were described as analogous to KHSO_4^0 species (Sverjensky et al., 1997), as was proposed by Wood and Samson (2000). Note that both H_2WO_4^0 and NaHWO_4^0 species are not supposed to be the dominant species in our calculations; thus, to take them into account, we used the independent data sources listed. The apparent Gibbs free energies of formation reaction for each tungsten species at pressure and temperature ($\Delta_r G^{TP}$) optimized with OptimA were converted into formation constants using the following relationship:

$$\Delta_r G^{TP} = -RT \cdot \ln K. \quad (8)$$

Then the formation constants obtained were described with the Bryzgalin–Ryzhenko (BR) model using the OptimC program (Table 4).

As the formation constants for NaWO_4^- and H_3WO_4^+ species are reported for the first time in this study, we report not only their optimized BR parameters but also their formation constants under experimental conditions as well as the uncertainty associated with their determination (Table S1, Fig. S1). Further details on the derivation of thermodynamic properties are provided in the Supplement. Note that in the absence of experimental data with different HCl concentrations and measurements at ambient temperature,

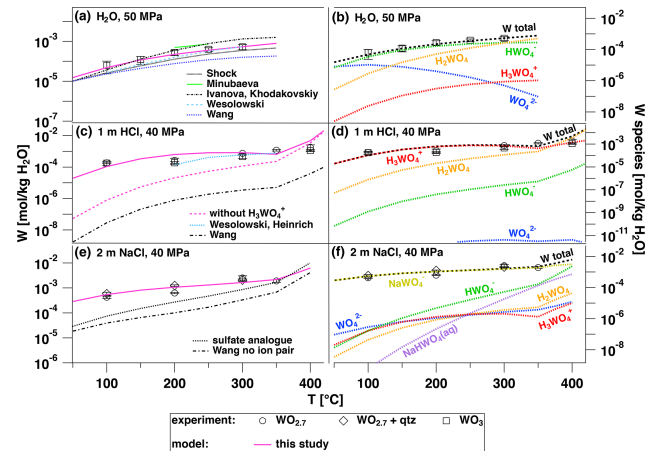


Figure 9. Results of thermodynamic modeling in comparison to the experimental in situ data as a function of temperature for the equilibration of W-oxides with fluid as indicated. Thermodynamic properties for WO_4^{2-} species were adopted from Shock et al. (1997) for all thermodynamic calculations. (a) WO_3 dissolved with H_2O – “Shock”: HWO_4^- HKF model by Shock et al. (1997); “Minubaeva”: HWO_4^- from constants reported by Minubaeva (2007); “Ivanova and Khodakovskiy”: HWO_4^- from constants reported by Ivanova and Khodakovskiy (1968, 1972); “Wesolowski”: HWO_4^- from constants reported by Wesolowski et al. (1984); “Wang”: HWO_4^- from Wang et al. (2019); “this study”: HWO_4^- BR model (Table 4), fit of the presented experimental data. For all experiments in pure water, the presence of H_2WO_4^0 (aq) does not affect the level of W solubility regardless of whether the thermodynamic data source considered this species. (b) Temperature dependence of W species in H_2O according to the model (this study). (c) WO_3 and $\text{WO}_{2.7}$ dissolved in 1 m HCl solution – “Wesolowski, Heinrich”: HWO_4^- from constants reported by Wesolowski et al. (1984) and H_2WO_4^0 (aq) constants from Heinrich (1990); “Wang”: HWO_4^- and H_2WO_4^0 (aq) BR model from Wang et al. (2019); “this study”: complexes from Table 4, including the new H_3WO_4^+ species; “without H_3WO_4^+ ”: complexes from Table 4, excluding the H_3WO_4^+ species. (d) Temperature dependence of W species in 1 m HCl solution (this study). (e) $\text{WO}_{2.7}$ dissolved in 2 m NaCl solution (\pm quartz) – “Wang no ion pair”: HWO_4^- and H_2WO_4^0 (aq) BR model from Wang et al. (2019), no NaHWO_4^0 and NaWO_4^- species, as proposed by Wang et al. (2019); “sulfate analogue”: species from Table 4 with the exception of NaHWO_4^0 (aq) and NaWO_4^- , which were calculated as having constants of formation reactions similar to $\text{K}^+ - \text{HSO}_4^{2-}$ and $\text{Na}^+ - \text{SO}_4^{2-}$. (f) Temperature dependence of W species in 2 m NaCl solution (this study).

the reported thermodynamic properties of H_3WO_4^+ species, having a structural formula of $[\text{H}_3\text{WO}_4^+] \cdot 2\text{H}_2\text{O}$, must be taken with caution and further research is needed to both improve calculations below 100 °C and discriminate H_3WO_4^+ from other potentially existing positively charged species, e.g., $[\text{WO}_2^{2+}] \cdot 4\text{H}_2\text{O}$.

4.4 Comparison of thermodynamic models to experimental data

Figure 9 shows the results of various thermodynamic models for the solubility of tungsten oxides, WO_3 or $\text{WO}_{2.7}$, in H_2O , 1 m HCl solution and 2 m NaCl solution as a function of temperature in comparison to experimental results from this study. In the case of H_2O , several models describe the experimental data. Particularly, experimental data and the model titled “Wesolowski”, which uses the classical species HWO_4^- (Wesolowski et al., 1984), H_2WO_4^0 (Heinrich, 1990) and WO_4^{2-} (Shock et al., 1997), match the experimental data very well, especially at temperatures above $250\text{ }^\circ\text{C}$, even though Wesolowski et al. (1984) performed their experiments only under vapor-saturated conditions. This implies that in the investigated range, pressure has a negligible effect. The model of Ivanova and Khodakovskiy (1968, 1972) matches better at temperatures below $250\text{ }^\circ\text{C}$. The stability constants of Wesolowski et al. (1984) for the reaction $\text{H}^+ + \text{WO}_4^{2-} = \text{HWO}_4^-$ are consistent with the thermodynamic data of Shock et al. (1997) and Ivanova and Khodakovskiy (1968, 1972) to within $\pm 5\text{ kJ mol}^{-1}$ for the apparent Gibbs free energy of formation of the HWO_4^- species. Consequently, all three models mentioned match the experimental results well, although the Shock et al. (1997) model shows slightly lower W concentrations. However, the model by Wang et al. (2019) clearly underestimates the experimental solubility data. The model developed in this study, which also introduces the H_3WO_4^+ species (see below), presents the fit of W concentrations with HWO_4^- species. As plotted in Fig. 9b, the dominant species above ca. $50\text{ }^\circ\text{C}$ is HWO_4^- , which controls the solubility. The modeled species is consistent with the interpretation of the XANES spectra measured at $300\text{ }^\circ\text{C}$ shown in Fig. 8, as discussed above.

Even though all models can be used to reproduce the experiments performed with H_2O , there are considerable discrepancies in the case of HCl solutions. In this case, all thermodynamic models strongly underestimate the experimentally determined W concentrations when using HWO_4^- , $\text{H}_2\text{WO}_{4(\text{aq})}$ and WO_4^{2-} species, as illustrated by the model of Wang et al. (2019) in Fig. 9c. The only model that agrees with the experimental data (between 200 and $350\text{ }^\circ\text{C}$) is the one titled “Wesolowski, Heinrich” in Fig. 9c, which used the WO_4^{2-} (Shock et al., 1997), HWO_4^- (Wesolowski et al., 1984) and $\text{H}_2\text{WO}_{4(\text{aq})}$ species (Heinrich, 1990). However, the usage of this combined model does not reproduce the data in the NaCl -bearing system and it cannot be extrapolated to temperatures below $200\text{ }^\circ\text{C}$. Addition of polymerized W species to the thermodynamic calculations using data introduced by Carocci et al. (2022) does not help either because these yield a W concentration in the form of polymers below 10^{-25} m W . Introducing the H_3WO_4^+ species, which was proposed by Bychkov and Zuykov (2005), solves the discrepancy, and Fig. 9d clearly shows that this species dominates the W species in the 0.1 m HCl solution over the complete

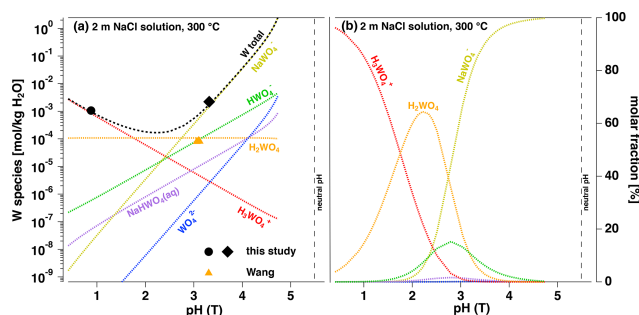


Figure 10. (a) Modeling of the pH dependence of $\text{WO}_{2.7}$ solubility for a 2 m NaCl solution using the species model developed in this study, in comparison to experimental data as indicated. (b) pH dependence of the W species according to the model.

temperature range investigated. The HWO_4^- species becomes dominant only at temperatures above $400\text{ }^\circ\text{C}$. Introducing the H_3WO_4^+ species not only solves the underestimation of solubility in the HCl solution but also is consistent with the data measured in H_2O , as its contribution to the solubility in H_2O is negligible (Fig. 9b).

For the NaCl -bearing solutions, two further species need to be considered. $\text{NaHWO}_{4(\text{aq})}$ and NaWO_4^- were proposed by Wood and Vlassopoulos (1989) and Wood and Samson (2000) (Table 4), whereas Wang et al. (2019) concluded that there is no effect of those species under hydrothermal conditions. The “Wang” model shown in Fig. 9e underestimates our experimental data. The other two models present two approaches to estimating the properties of ion pairs with tungsten. The model titled “sulfate analogue” depicts the approach proposed by Wood and Samson (2000), which assumes that the formation constants of $\text{NaHWO}_{4(\text{aq})}$ and NaWO_4^- are equal to KHSO_4^0 (Sverjensky et al., 1997) and NaSO_4^- (Pokrovski et al., 1995), respectively. The model titled “this study”, representing the one that is based on the fit of our experimental solubility data in NaCl -bearing solutions using NaWO_4^- species, agrees best with the experimental data. The results of this optimization are reported in Table S1 and summarized in Table 4 with the resulting BR model parameters. Note that our solubility data may be quantitatively described using either neutral NaHWO_4^0 aqueous species or charged NaWO_4^- complex. However, we favor the choice of NaWO_4^- because, first, the sulfate analogue model showed that NaWO_4^- species should be much more abundant than $\text{NaHWO}_{4(\text{aq})}$ in our NaCl -bearing experiments and, second, the fit of experiments using the $\text{NaHWO}_{4(\text{aq})}$ species gave unphysical values for the association constants. These cannot be higher than the estimated values of the NaWO_4^- species (see Table S5). The addition of the H_3WO_4^+ species in our model does not influence the calculated results in NaCl -bearing systems, which is similar to the experiments in pure water. Also note that the addition of quartz to the calculations has no effect on the W solubilities.

In Fig. 10 we provide modeled data on the effect of pH on the solubility of $\text{WO}_{2.7}$ in a 2 m NaCl solution at 300 °C in comparison to our experimental data and one data point of Wang et al. (2019). The solubility shows a clear minimum at $\text{pH}(T) = 2.5$ of about 10^{-4} m W. At $\text{pH}(T)$ of 1.0 and 5.6, ca. 10^{-3} m W and ca. 1 m W are calculated, respectively. The comparison to the experimental data of this study provides a very good match. However, the data point of Wang et al. (2019) is lower by almost 1 order of magnitude. This discrepancy and the underestimation of the model by Wang et al. (2019) for their runs in H_2O may indicate an incomplete recovery of W after the quenched experiments that might cause an underestimation of W concentrations in experimental conditions. We also suggest that the fact that solids and solution were isolated by quartz wool in experiments of Wang et al. (2019) might also have led to incomplete equilibration.

Figure 10b documents that the new H_3WO_4^+ species dominates the solubility at $\text{pH}(T)$ below 2.1. At higher pH, NaWO_4^- becomes more abundant. The XANES spectra corresponding to the two data points plotted in Fig. 10 indicate distorted octahedral W species for both runs (Fig. 8). Both solubility runs were performed in acidic conditions, and thus, the assignments are consistent with the pH-dependent EXAFS observations of Hoffmann et al. (2000). Consequently, we may infer that the NaWO_4^- species has octahedral molecular symmetry at acidic pH levels. However, a final answer needs to be found using spectroscopic data of better quality.

A final test for the proposed thermodynamic model that includes the H_3WO_4^+ species and ion pairs was performed by modeling the scheelite and ferberite solubility, which are the most important ore minerals for W. The result is shown in Fig. 11. In the case of scheelite, the model is directly compared to the in situ data of this study. Even though not explicitly shown, the H_3WO_4^+ and H_2WO_4^0 species are not relevant in the HCl-free systems. The modeled concentrations for scheelite agree well with the experimental ones. The W species is dominated by WO_4^{2-} and HWO_4^- in H_2O at 100 °C. With increasing temperature, the concentration of the HWO_4^- species increases. As soon as NaCl is added, NaWO_4^- becomes the most dominant species. It should be noted that the scheelite solubility strongly increases with NaCl concentration below 1 m NaCl and levels off at higher NaCl concentrations. For ferberite, the picture is slightly different. Below 200 °C, the ferberite solubility is lower than that of scheelite by almost 2 orders of magnitude. At higher temperatures, the ferberite solubility approaches that of scheelite. The results of our modeling suggest that wolframite is the most likely mineral to crystallize in Fe-bearing systems, particularly at temperatures of 100–350 °C. It is worth mentioning that the absolute difference between scheelite and ferberite solubility is mostly related to differences in their thermodynamic stability and that the different dependence on NaCl concentration (especially at high T , Fig. 11c and d) is related to the influence of chloride com-

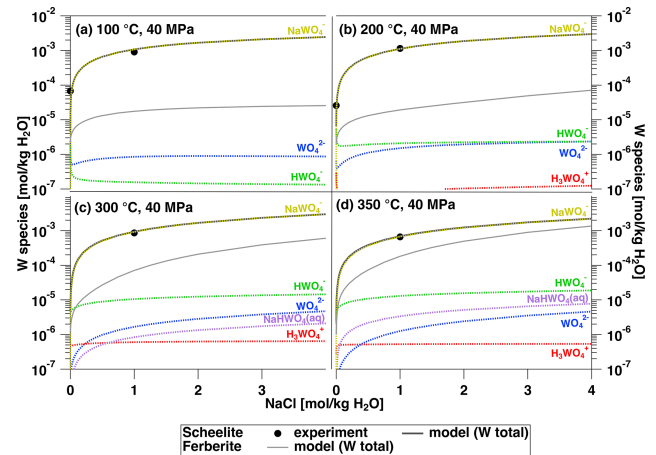


Figure 11. Modeling of the total W concentration in the fluid in equilibrium with scheelite as a function of NaCl content using the species model developed in this study for the pressure and temperature conditions indicated. Species model: WO_4^{2-} , Shock et al. (1997); HWO_4^- , H_2WO_4^0 , H_3WO_4^+ , NaHWO_4^0 and NaWO_4^- from Table 4. In addition, the total W concentration in equilibrium with ferberite is superimposed for comparison.

plexation or ion pairing on the Ca^{2+} and Fe^{2+} activity in the fluid.

In essence, the newly introduced model shows that we can describe the solubility of W for fluids in the presence of WO_3 , $\text{WO}_{2.7}$ or CaWO_4 using the H_3WO_4^+ , H_2WO_4^0 , HWO_4^- and WO_4^{2-} species in Na-free systems. In Na-bearing systems, the NaHWO_4^0 and then NaWO_4^- have to be considered as well. The W concentrations in our experiments did not exceed 10^{-3} m W, so the polymerized species found in previous studies (e.g., Carocci et al., 2022) have no importance. The situation apparently changes for Na-rich HCl solutions, i.e., in the case of solutions made by dissolving $\text{Na}_2\text{WO}_4 \cdot 2\text{H}_2\text{O}$. Here, polymerized W species are formed at low pH levels, especially at low temperature as outlined not only by Carocci et al. (2022) but also by earlier studies (e.g., Hoffmann et al., 2000; Dewan and Kepert, 1973). Under these low-pH conditions, even in the presence of NaCl, the presence of the polymerized W species leads to incongruent dissolution of scheelite (Carocci et al., 2022).

4.5 Geochemical implications

Our experimental W solubilities compare well with the range of W concentrations found in natural fluids. Naumov et al. (2011) report general physiochemical parameters of the formation of hydrothermal tungsten deposits based on fluid and melt inclusion studies of 253 tungsten and tungsten–tin deposits worldwide, without specifying differences in the formation conditions of ore deposits. According to their database, the majority of W hydrothermal ore deposits are formed at temperatures between 200 and 400 °C

with maxima at 200–300 °C at a low to moderate salinity of ≤ 10 wt % NaCl_{eq.} and pressures between 50 and 150 MPa. The geometric mean W concentration in mineral-forming fluids reported by Naumov et al. (2011) is $30 \mu\text{g g}^{-1}$ (with a complete range of 25 to $144 \mu\text{g g}^{-1}$), which is equivalent to $10^{-4} \text{ mol kg}^{-1} \text{ H}_2\text{O}$. More recently, Lecumberri-Sanchez et al. (2017) have reported 1–70 $\mu\text{g g}^{-1}$ W in low-salinity (5 wt %–8 wt % NaCl_{eq.}) fluid inclusions of horizontally oriented veins with wolframite precipitation in Panasqueira (Portugal). Finally, Korges et al. (2018) studied the Zinnwald–Cínovec deposit, Erzgebirge (Ore Mountains, Germany). Here, wolframite is also found predominantly in subhorizontal quartz-rich veins. Four primary fluid inclusion types were identified that differ in homogenization temperatures and salinities. The majority of fluid inclusions suggest formation of these deposits at 300–360 °C and variable salinities (1 wt %–14 wt % NaCl_{eq.}). Tungsten concentrations of fluid inclusions entrapped in quartz and cassiterite range mostly between 100–600 $\mu\text{g g}^{-1}$ but show large scatter (a few to several thousand micrograms per gram even within the same type of inclusion) and no correlation with temperature or salinity of the individual fluid inclusion. Similar W concentrations are reported for tourmaline-hosted fluid inclusions in the biotite–muscovite pegmatites of the Karagwe–Ankole belt in Rwanda (5–575 $\mu\text{g g}^{-1}$ W; Hulsbosch et al., 2016) and for the Cryo-Genie pegmatite, USA (40–400 $\mu\text{g g}^{-1}$ W; Sirbescu et al., 2013).

The most important W ore minerals are scheelite (CaWO₄) and wolframite ((Fe,Mn)WO₄), whose precipitation depends not only on the activity of tungstate species but also on the activity of Ca²⁺, Fe²⁺ and Mn²⁺ in the fluid. At low activity levels of these components, W can be efficiently transported by fluids that carry sufficient alkali-chloride contents and are close to neutral pH. Increasing alkalinity would further enhance W solubility in the fluid due to the stabilization of the WO₄²⁻ species. Once fluids that carry a significant amount of W interact with a Ca- and (Fe,Mn)-rich host rock, the solubility product of scheelite or wolframite is reached and these minerals will begin to precipitate. Lecumberri-Sanchez et al. (2017) and Korges et al. (2018) described mineralization textures of wolframite related to quartz-rich veins, which strongly suggest precipitation of wolframite due to fluid–rock interaction and associated changes in pH and the major element composition of the fluid. In both cases, dark mica (biotite or zinnwaldite) may have served as a source for Fe. In Panasqueira, pH changes are thought to be induced by the reaction of white mica with the fluid (Lecumberri-Sanchez et al., 2017), whereas at Zinnwald, crack opening and boiling are suggested to have induced pH changes (Korges et al., 2018; Qiao et al., 2024). With the improved thermodynamic model of the W fluid species presented here, these complex interactions may now be traced and quantified. In fluids with low Ca and Fe but considerable NaCl concentrations, W contents in the fluids may reach $10^{-3} m$ W before tungsten oxides precipitate (Fig. 8). There is a strong effect

of pH with a minimum in solubility of W-oxide in intermediate acidic conditions (Fig. 9). In the case of wolframite, the presence of Fe and/or Mn, as well as cooling, will lead to a fluid in which the solubility product of wolframite will be reached first (Fig. 10). Further, lowering of NaCl concentrations or lowering of pH may facilitate wolframite precipitation. In the case of scheelite, our model shows that buffered W contents in fluids become almost independent of the NaCl concentrations above 1 m NaCl, but they strongly depend on NaCl concentrations below this threshold. Thus, a change in both pH and NaCl concentration will promote scheelite precipitation upon fluid–rock interaction or fluid mixing. These conditions may have been met in and around the world-class Felbertal deposit, where hydrothermal magmatic fluids interacted with a Ca-rich host rocks dominated by metabasites (e.g., Kozlik and Raith, 2017). Particularly, the Sn–W skarn formation at Messelingscharte described by Ordosch et al. (2019) represents an extreme case with several phases of scheelite growth and recrystallization. Scheelite mineralization is further complicated by the presence of fluorine, which has been suggested to have mobilized and enriched rare-earth elements (REE) and high-field-strength elements (HFSE) in the Felbertal complex (Kozlik and Raith, 2017; Ordosch et al., 2019). Wang et al. (2021) reported enhanced W solubility with increasing fluorine concentrations and identified an F-bearing W species in the fluid as dominant under acidic conditions. They further suggest that the competing stability of fluorite and scheelite will determine whether wolframite or scheelite is the ore-forming mineral. However, this F-bearing species remains to be identified through in situ spectroscopy.

In conclusion, we used W concentrations in fluids that were experimentally determined in situ at high pressures and temperatures to constrain thermodynamic parameters for W solubility and W fluid species. With these, we were able to introduce the H₃WO₄⁺ species that is dominant in acidic fluids and we have also improved thermodynamic parameters of other Na-bearing W species, providing a set of fluid species that cover a wide range of fluid compositions, which is necessary for understanding the complex processes of W enrichment and mineralization in hydrothermal systems. However, there is still a lot to do, as the uncertainties in thermodynamic properties are still large, and they need to be improved by further experiments to better constrain, for example, the pressure dependence of W solubility and fundamental thermodynamic functions (G , H , S , C_p and V) of W species in reference conditions (25 °C, 1 bar) that will serve as the basis for more accurate thermodynamic models.

Data availability. The data of Figs. 2 to 11 and Table 3 are available at the data repository at <https://dataservices-cms.gfz.de>: GFZ Data Services, <https://doi.org/10.5880/figeo.d.2024.002> (Borchert et al., 2024).

Supplement. The supplement related to this article is available online at <https://doi.org/10.5194/ejm-37-111-2025-supplement>.

Author contributions. MW, MB, ML, MAK, AL, EW, RAA and DT performed *in situ* XAS experiments; RAA analyzed solid products after experiments with XRD, scanning electron microscopy (SEM) and electron probe microanalysis (EPMA); MW and MB analyzed the solubility and XANES and EXAFS data; MAK and EFB performed the thermodynamic modeling of the solubility results; all co-authors contributed to writing the manuscript.

Competing interests. The contact author has declared that none of the authors has any competing interests.

Disclaimer. Publisher's note: Copernicus Publications remains neutral with regard to jurisdictional claims made in the text, published maps, institutional affiliations, or any other geographical representation in this paper. While Copernicus Publications makes every effort to include appropriate place names, the final responsibility lies with the authors.

Acknowledgements. We acknowledge DESY (Hamburg, Germany), a member of the Helmholtz Association (HGF), for the provision of experimental facilities and access to beamtime. Parts of this research were carried out at DESY beamline P65, and we would like to thank Wolfgang Caliebe (P64), Matthias Herrmann and Ruidy Nemausat for their excellent support at the beamline; R. Biller for technical support with the autoclave; and Claudia Schwan and Anca Ciobano for generous help and sterling assistance in the chemical laboratories at DESY. Parts of this research were carried out at FAME at ESRF, France, and our sincere thanks go to the FAME staff for excellent support as well as to ESRF for providing access to beamtime and financial support. We also thank Michael Feldhaus, Peter Weitkamp and Arno Rohrbach (all Universität Münster) for support and Christina Günter, Christoph Moeller and Thomas Block (Universität Potsdam) for help with high-temperature synthesis, XRD and Raman characterization of W-oxides. We are grateful to Gleb Pokrovski (GET-OMP, Toulouse, France) and Christian Schmidt (GFZ, Potsdam, Germany) for very helpful discussions about thermodynamic modeling and tungsten aqueous speciation. Comments from Max Korges on the manuscript are highly appreciated.

Financial support. Maria A. Kokh, Max Wilke and Stephan Klemme were supported by the Deutsche Forschungsgemeinschaft (WI 2000/25-1, KL 1368/13-1). Stephan Klemme received funding from the Bundesministerium für Bildung und Forschung (FKZ 05K16PMA). This research was supported by the Centre for Molecular Water Science (CMWS) in an Early Science Project.

Review statement. This paper was edited by Rucheng Wang and reviewed by Gleb Pokrovski and one anonymous referee.

References

- Akinfiev, N. N. and Diamond, L. W.: Thermodynamic description of aqueous nonelectrolytes at infinite dilution over a wide range of state parameters, *Geochim. Cosmochim. Acta*, 67, 613–629, 2003.
- Barin, I. (Ed.): *Thermochemical Data of Pure substances*. VCH Verlagsgesellschaft mbH, Weinheim, Germany, ISBN 3-527-28745-0, 1995.
- Barin, I. and Knacke, O. (Eds.): *Thermochemical properties of inorganic substances*: Berlin, Springer-Verlag, 921 pp., 1973.
- Bianconi, A., Dell'Ariceia, M., Gargano, A., and Natoli, C. R.: Bond length determination using XANES, in: *EXAFS and Near Edge Structure*, edited by: Bianconi, A., Incoccia, L., and Stilplich, S., Springer Series in Chemistry and Physics, Berlin, 27, 57–61, 1983.
- Borchert, M., Kokh, M. A., Louvel, M., Bazarkina, E. F., Loges, A., Testemale, D., Al Abed, R., Klemme, S., and Wilke, M.: Tungsten concentrations and tungsten EXAFS and XANES data in hydrothermal solutions, GFZ Data Services [data set], <https://doi.org/10.5880/figeo.d.2024.002>, 2024.
- Borg, S., Liu, W., Etschmann, B., Tian, Y., and Brugger, J.: An XAS study of molybdenum speciation in hydrothermal chloride solutions from 25–385 °C and 600 bar, *Geochim. Cosmochim. Acta*, 92, 292–307, 2012.
- Brugger, J., Liu, W., Etschmann, B., Mei, Y., Sherman, D. M., and Testemale, D.: A review of the coordination chemistry of hydrothermal systems, or do coordination changes make ore deposits?, *Chem. Geol.*, 447, 219–253, 2016.
- Bryzgalin, O. V. and Rafal'sky, R. P.: Estimation of instability constants for ore-element complexes at elevated temperatures, *Geochem. Intern.*, 19, 839–849, 1982.
- Bychkov, A. Y. and Zuykov, V. V.: Solubility of tungstic acid and forms of tungsten transport in sodium chloride solutions at 25 °C, *Dokladi akademii nauk*, 400, 69–71, 2005.
- Carocci, E., Truche, L., Cathelineau, M., Caumon, M. C., and Bazarkina, E. F.: Tungsten (VI) speciation in hydrothermal solutions up to 400 °C as revealed by *in situ* Raman spectroscopy, *Geochim. Cosmochim. Acta*, 317, 306–324, 2022.
- Crerar, D. A., Wood, S., Brantley, S., and Bocarsly, A.: Chemical controls on solubility of ore-forming minerals in hydrothermal systems, *Can. Mineral.*, 23, 333–352, 1985.
- Dewan, J. C. and Kepert, D. L.: Rapid Acidification of Solutions containing Tungstate Anions, *J. Chem. Soc., Dalton Transactions*, 224–225, 1973.
- Diehl, R., Brandt, G., and Salje, E.: The crystal structure of triclinic WO₃, *Acta Cryst.*, B34, 1105–1111, 1978.
- Driesner, T.: The System H₂O-NaCl. II. Correlations for molar volume, enthalpy, and isobaric heat capacity from 0 to 1000 degrees C, 1 to 5000 bar, and 0 to 1 X_{NaCl}, *Geochim. Cosmochim. Acta*, 71, 4902–4919, 2007.
- Driesner, T. and Heinrich, C. A.: The System H₂O-NaCl. I. Correlation Formulae for Phase Relations in Temperature-Pressure-Composition Space from 0 to 1000 °C, 0 to 5000 bar, and 0 to 1 X_{NaCl}, *Geochim. Cosmochim. Acta*, 71, 4880–4901, 2007.
- Elam, W. T., Ravel, B. D., and Sieber, J. R.: A new atomic database for X-ray spectroscopic calculations, *Rad. Phys. Chem.*, 63, 121–128, 2002.

- Farrugia, L. J.: Sodium tungstate dihydrate: a redetermination, *Acta Cryst.*, E63, i142, <https://doi.org/10.1107/S1600536807023355>, 2007.
- Franck, E. U., Rosenzweig, S., and Christoforakos, M.: Calculation of the dielectric constant of water to 1000 °C and very high pressures, *Bunsen-Ges. Phys. Chem.*, 94, 199–203, 1990.
- Fuggle, J. C. and Mårtensson, N.: Core-level binding energies in metals, *J. Electron. Spectrosc. Relat. Phenom.*, 21, 275–281, [https://doi.org/10.1016/0368-2048\(80\)85056-0](https://doi.org/10.1016/0368-2048(80)85056-0), 1980.
- Gibert, F., Moine, B., Schott, J., and Dandurand, J. L.: Modeling of the transport and deposition of tungsten in the scheelite-bearing calc-silicate gneisses of the Montagne Noire, France, *Contrib. Mineral. Petrol.*, 112, 371–384, 1992.
- Han, B., Khoroshilov, A., Tyurin, A., Baranchikov, A., Razumov, M., Ivanova, O., Gavrichev, K., and Ivanov, V.: WO₃ thermodynamic properties at 80–1256 K revisited, *Chem. J. Therm. Anal. Calo.*, 142, 1533–1543, 2020.
- Han, Z., Golev, A., and Edraki, M.: A Review of Tungsten Resources and Potential Extraction from Mine Waste, *Minerals*, 11, 701, <https://doi.org/10.3390/min11070701>, 2021.
- Heinrich, C. A.: The chemistry of hydrothermal tin (-tungsten) ore deposits, *Econ. Geol.*, 85, 457–481, 1990.
- Helgeson, H. C. and Kirkham, D. H.: Theoretical prediction of the thermodynamic behavior of aqueous electrolytes at high pressures and temperatures; I, Summary of the thermodynamic/electrostatic properties of the solvent, *Am. J. Sci.*, 274, 1089–1198, 1974.
- Helgeson, H. C., Kirkham, D. H., and Flowers, G. C.: Theoretical prediction of thermodynamic behavior of aqueous electrolytes at high temperatures and pressures. IV. Calculation of activity coefficients, osmotic coefficients, and apparent molal and standard and relative partial molal properties to 5 kb and 600 °C, *Am. J. Sci.*, 281, 1249–1516, 1981.
- Hoffmann, M. M., Darab, J. G., Heald, S. M., Yonker C. R., and Fulton J. L.: New experimental developments for in situ XAFS studies of chemical reactions under hydrothermal conditions, *Chem. Geol.*, 167, 89–103, 2000.
- Hulsbosch, N., Boiron, M.-Ch., Dewaele, S., and Muecher, P.: Fluid fractionation of tungsten during granite-pegmatite differentiation and the metal source of peribatholithic W quartz veins: Evidence from the Karagwe-Ankole Belt (Rwanda), *Geochim. Cosmochim. Acta*, 175, 299–318, 2016.
- Ivanova, G. F. and Khodakovskiy, I. L.: Chemical forms of tungsten transport in hydrothermal solutions, *Geokhimiya*, 8, 426, 1968 (in Russian).
- Ivanova, G. F. and Khodakovskiy, I. L.: About chemical state of tungsten in hydrothermal solutions, *Geokhimiya*, 11, 1426–1433, 1972 (in Russian).
- Johnson, J. W., Oelkers, E. H., and Helgeson, H. C.: SUPCRT92: a software package for calculating the standard molal thermodynamic properties of minerals, gases, aqueous species, and reactions from 1 to 5000 bar and 0 to 1000 °C, *Comput. Geosci.*, 18, 899–947, 1992.
- Kestin, J., Sengers, J. V., Kamgar-Parsi, B., and Sengers J. M. H. L.: Thermophysical properties of fluid H₂O, *J. Phys. Chem. Ref. Data*, 13, 175–183, 1984.
- Klemme, S., Feldhaus, M., Potapkin, V., Wilke, M., Borchert, M., Louvel, M., Loges, A., Rohrbach, A., Weitkamp, P., Welter, E., Kokh, M., Schmidt, C., and Testemale, D.: A hydrothermal apparatus for x-ray absorption spectroscopy of hydrothermal fluids at DESY, *Rev. Sci. Instrum.*, 92, 063903, <https://doi.org/10.1063/5.0044767>, 2021.
- Klimek, P., Obersteiner, M., and Thurner, S.: Systemic trade risk of critical resources, *Sci. Adv.*, 1, e1500522, <https://doi.org/10.1126/sciadv.1500522>, 2015.
- Korges, M., Weis, P., Lüders, V., and Laurent, O.: Depressurization and boiling of a single magmatic fluid as a mechanism for tungsten deposit formation, *Geology*, 46, 75–78, 2018.
- Kozlik, M. and Raith, J.: Variscan metagranitoids in the central Tauern Window (Eastern Alps, Austria) and their role in the formation of the Felbertal scheelite deposit, *Lithos*, 278–281, 303–320, 2017.
- Kwak, T. A. P.: W-Sn skarn deposits and related metamorphic skarns and granitoids, in: *Developments in Economic Geology*, 24, Amsterdam, Elsevier Science, 468 pp., 1987.
- Lecumberri-Sanchez, P., Vieira, R., Heinrich, C. A., Pinto, F., and Wälle, M.: Fluid-rock interaction is decisive for the formation of tungsten deposits, *Geology*, 45, 579–582, 2017.
- Lemmon, E. W., McLinden, M. O., and Friend, D. G.: Thermophysical Properties of Fluid Systems, in: *NIST Chemistry WebBook*, edited by: Linstrom, P. J. and Mallard, W. G., NIST Standard Reference Database. National Institute of Standards and Technology, Gaithersburg MD, <https://doi.org/10.18434/T4D303>, 2019.
- Li, G., Bridges, F., and Brown, G. S.: Multielectron X-ray photoexcitation observations in X-ray-absorption fine-structure background, *Phys. Rev. Lett.*, 68, 1609–1612, 1992.
- Marshall, W. L. and Franck, E. U.: Ion product of water substance, 0–1000 °C, 1–10,000 bars new international formulation and its background, *J. Phys. Chem. Ref. Data*, 10, 295–304, 1981.
- Mei, Y., Liu, W., Guan, O., Brugger, J., Etschmann, B., Siégel, C., Wykes, J., and Ram, R.: Tungsten speciation in hydrothermal fluids, *Geochim. Cosmochim. Acta*, <https://doi.org/10.1016/j.gca.2024.06.030>, in press, 2024.
- Minubaeva, Z.: UV Spectroscopic Studies of the Hydrothermal Geochemistry of Molybdenum and Tungsten, PhD Thesis, ETH Zurich, 142 pp., <https://doi.org/10.3929/ethz-a-005557770>, 2007.
- Naumov, V. B., Dorofeev, V. A., and Mironova, O. F.: Physicochemical parameters of the formation of hydrothermal deposits: A fluid inclusion study. I. Tin and tungsten deposits, *Geochem. Int.*, 49, 1002–1021, 2011.
- Oelkers, E. H. and Helgeson, H. C.: Triple-ion anions and polynuclear complexing in supercritical electrolyte solutions, *Geochim. Cosmochim. Acta*, 54, 727–738, 1990.
- Oelkers, E. H. and Helgeson, H. C.: Calculation of activity coefficients and degrees of formation of neutral ion pairs in supercritical electrolyte solutions, *Geochim. Cosmochim. Acta*, 55, 1235–1251, 1991.
- Ordosch, A., Raith, J. G., Schmidt, S., and Aupers, K.: Polyphase scheelite and stanniferous silicates in a W-(Sn) skarn close to Felbertal tungsten mine, Eastern Alps, *Mineral. Petrol.*, 113, 703–725, 2019.
- Pearson, R. G.: Hard and soft acids and bases, *Am. Chem. Soc. J.*, 85, 3533–3539, 1963.
- Perrin, D. D.: Dissociation constants of inorganic acids and bases in aqueous solution, Butterworth & Co., London, 112 pp., ISBN 978-0408700153, 1969.

- Pokrovski, G. S., Schott, J., and Sergeev, A. S.: Experimental determination of the stability constants of NaSO_4^- and NaB(OH)_4^0 in hydrothermal solutions using a new high-temperature sodium-selective glass electrode – Implications for boron isotopic fractionation, *Chem. Geol.*, 124, 253–265, 1995.
- Pokrovski, G. S., Roux, J., Hazemann, J.-L., and Testemale, D.: An X-ray absorption spectroscopy study of argutite solubility and aqueous Ge(IV) speciation in hydrothermal fluids to 500 °C and 400 bar, *Chem. Geol.*, 217, 127–145, 2005.
- Proux, O., Biquard, X., Lahera, E., Menthonnex, J.-J., Prat, A., Ulrich, O., Soldo, Y., Trevisson, P., Kapoujyan, G., Perroux, G., Taunier, P., Grand, D., Jeantet, P., Deleglise, M., Roux, J.-P., and Hazemann, J.-L.: FAME: a new beamline for X-ray absorption investigations of very diluted systems of environmental, material and biological interests, *Phys. Scr.*, T115, 970–973, 2005.
- Proux, O., Nassif, V., Prat, A., Ulrich, O., Lahera, E., Biquard, X., Menthonnex, J.-J., and Hazemann, J.-L.: Feedback system of a liquid-nitrogen-cooled double-crystal monochromator: design and performances, *J. Synchrotron Rad.*, 13, 59–68, 2006.
- Qiao, S., Loges, A., and John, T.: Formation of topaz-greisen by a boiling fluid: a case study from the Sn-W-Li deposit, Zinnwald/Cínovec, *Econ. Geol.*, 119, 805–828, 2024.
- Rafal'sky, R. P., Bryzgalin, O. V., and Fedorov, P. L.: Transport of tungsten and scheelite deposition under hydrothermal conditions, *Geochem. Intern.*, 5, 611–624, 1984.
- Rehr, J. J., Kas, J. J., Vila, F. D., Prange, M. P., and Jorissen, K.: Parameter-free calculations of x-ray spectra with FEFF9, *Phys. Chem. Chem. Phys.*, 12, 5503–5513, 2010.
- Robie, R. A. and Hemingway, B. S.: Thermodynamic properties of minerals and related substances at 298.15 K and 1 Bar (10^5 Pascals) pressure and at higher temperatures, U.S., Geological Survey Bulletin, 2131, 1995.
- Ryzhenko, B. N., Bryzgalin, O. V., Artamkina, I. Y., Spasennykh, M. Y., and Shapkin, A. I.: An electrostatic model for the electrolytic dissociation of inorganic substances dissolved in water, *Geochem. Int.*, 22, 128–144, 1985.
- Seward, T. M.: Metal complex formation in aqueous solutions at elevated temperatures and pressures, *Phys. Chem. Earth*, 13–14, 113–132, 1981.
- Seward, T. M. and Barnes, H. L.: Metal transport by hydrothermal ore fluids, in: *Geochemistry of Hydrothermal Ore Deposits*, edited by: Barnes, H. L., John Wiley & Sons, New York, 435–486, <https://doi.org/10.5860/choice.35-2126>, 1997.
- Shock, E. L., Sassani, D. C., Willis, M., and Sverjensky, D. A.: Inorganic species in geologic fluids: Correlations among standard molal thermodynamic properties of aqueous ions and hydroxide complexes, *Geochim. Cosmochim. Acta*, 61, 907–950, 1997.
- Shvarov, Y. V.: HCh: new potentialities for the thermodynamic simulation of geochemical systems offered by Windows, *Geochem. Intern.*, 46, 834–839, 2008.
- Shvarov, Y. V.: A suite of programs, OptimA, OptimB, OptimC, and OptimS compatible with the Unitherm database, for deriving the thermodynamic properties of aqueous species from solubility, potentiometry and spectroscopy measurements, *Appl. Geochem.*, 55, 17–27, 2015.
- Shvarov, Y. V. and Bastrakov, E.: HCh: a software package for geochemical equilibrium modelling, User's Guide, Australian Geological Survey Organization, record 25, 1999.
- Sirbescu, M.-L., Krukowski, E. G., Schmidt, C., Thomas, R., Samson, I. M., and Bodnar, R. J.: Analysis of boron in fluid inclusions by microthermometry, laser ablation ICP-MS, and Raman spectroscopy: Application to the Cryo-Genie Pegmatite, San Diego County, California, USA, *Chem. Geol.*, 342, 138–150, 2013.
- Sverjensky, D. A., Shock, E. L., and Helgeson, H. C.: Prediction of the thermodynamic properties of aqueous metal complexes to 1000 °C and 5 kb, *Geochim. Cosmochim. Acta*, 61, 1359–1412, 1997.
- Sverjensky, D. A., Harrison, B., and Azzolini, D.: Water in the deep Earth: the dielectric constant and the solubilities of quartz and corundum to 60 kb and 1200 C, *Geochim. Cosmochim. Acta*, 129, 125–145, 2014.
- Tagirov, B. R., Zotov, A. V., and Akinfiyev, N. N.: Experimental study of dissociation of HCl from 350 to 500 °C and from 500 to 2500 bars: Thermodynamic properties of HCl^0 (aq), *Geochim. Cosmochim. Acta*, 61, 4267–4280, 1997.
- Tanger, J. C. and Helgeson, H. C.: Calculation of the thermodynamic and transport properties of aqueous species at high pressures and temperatures; revised equations of state for the standard partial molal properties of ions and electrolytes, *Am. J. Sci.*, 288, 19–98, 1988.
- Testemale, D., Argoud, R., Geaymond, O., and Hazemann, J.-L.: High pressure/high temperature cell for x-ray absorption and scattering techniques, *Rev. Sci. Instrum.*, 76, 043905, <https://doi.org/10.1063/1.1884188>, 2005.
- Testemale, D., Brugger, J., Liu, W., Etschmann, B., and Hazemann, J.-L.: In-situ X-ray absorption study of Iron (II) speciation in brines up to supercritical conditions, *Chem. Geol.*, 264, 295–310, 2009.
- Testemale, D., Prat, A., Lahera, E., and Hazemann, J.-L.: Novel high-pressure windows made of glass-like carbon for x-ray analysis, *Rev. Sci. Instrum.*, 87, 075115, <https://doi.org/10.1063/1.4959110>, 2016.
- Testemale, D., Pokrovski, G.S., Lahera, E., Prat, A., Kieffer, I., Delnet, W., Proux, O., Louvel, M., Sanchez-Valle, C., and Hazemann, J. L.: In situ X-ray absorption spectroscopy using the FAME autoclave: a window into fluid-mineral-melt interactions in the Earth's crust, *High Pressure Res.*, 44, 277–293, 2024.
- Wang, X., Qui, Y., Chou, I.-M., Zhang, R., Li, G., and Zhong, R.: Effects of pH and salinity on the hydrothermal transport of tungsten: insights from in situ Raman spectroscopic characterization of $\text{K}_2\text{WO}_4\text{-NaCl-HCl-CO}_2$ solutions at temperatures up to 400 °C, *Geofluids*, 2020, 2978984, <https://doi.org/10.1155/2020/2978984>, 2020a.
- Wang, X., Qui, Y., Lu, J., Chou, I.-M., Zhang, W., Li, G., Hu, W., Li, Z., and Zhong, R.: *In situ* Raman spectroscopic investigation of the hydrothermal speciation of tungsten: implication for the ore-forming process, *Chem. Geol.*, 532, 119299, <https://doi.org/10.1016/j.chemgeo.2019.119299>, 2020b.
- Wang, X. S., Timofeev, A., Williams-Jones, A. E., Shang, L. B., and Bi, X. W.: An experimental study of the solubility and speciation of tungsten in NaCl-bearing aqueous solutions at 250, 300, and 350 °C, *Geochim. Cosmochim. Acta*, 265, 313–329, 2019.
- Wang, X. S., Williams-Jones, A. E., Hu, R. Z., Shang, L. B., and Bi, X. W.: The role of fluorine in granite-related hydrothermal tungsten ore genesis: Results of experiments and modeling, *Geochim. Cosmochim. Acta*, 292, 170–187, 2021.

- Welter, E., Chernikov, R., Herrmann, M., and Nemausat, R.: A beamline for bulk sample X-ray absorption spectroscopy at a high brilliance storage ring PETRA III, AIP Conf. Prog., 2054, 040002, <https://doi.org/10.1063/1.5084603>, 2019.
- Wesolowski, D., Drummond, S. E., Mesmer, R. E., and Ohmoto, H.: Hydrolysis equilibria of tungsten (VI) in aqueous sodium-chloride solutions to 300 °C, Inorg. Chem., 23, 1120–1132, 1984.
- Wilke, M., Farges, F., Partzsch, G. M., Schmidt, C., and Behrens, H.: Speciation of Fe in silicate glasses and melts by *in situ* XANES spectroscopy, Am. Mineral., 92, 44–56, 2007.
- Winterer, M.: *xafsX*: a program to process, analyse and reduce X-ray absorption fine structure spectra (XAFS), in: *International Tables for Crystallography*, Vol I: X-ray Absorption Spectroscopy and Related Techniques, edited by: Chantler, C. T., Bunker, B., and Boscherini, F., <https://doi.org/10.1107/s1574870720003481>, 2022.
- Wood, S. A.: Experimental determination of the solubility of WO_3 (s) and the thermodynamic properties of H_2WO_4 (aq) in the range 300–600 °C at 1 kbar: calculation of scheelite solubility, Geochim. Cosmochim. Acta, 56, 1827–1836, 1992.
- Wood, S. A. and Samson, I. M.: The hydrothermal geochemistry of tungsten in granitoid environments: I. Relative solubilities of ferberite and scheelite as a function of T, P, pH, and m NaCl, Econ. Geol., 95, 143–182, 2000.
- Wood, S. A. and Vlassopoulos, D.: Experimental determination of the hydrothermal solubility and speciation of tungsten at 500 °C and 1 kbar, Geochim. Cosmochim. Acta, 53, 303–312, 1989.
- Xiao, L., Ji, L., Yin, C., Chen, A., Chen, X., Liu, X., Li, J., Sun, F., and Zhao, Z.: Tungsten extraction from scheelite hydrochloric acid decomposition residue by hydrogen peroxide, Miner. Eng., 179, 107461, <https://doi.org/10.1016/j.mineng.2022.107461>, 2022.
- Zalkin, A. and Templeton, D. H.: X-ray diffraction refinement of the calcium tungstate structure, J. Chem. Phys., 40, 501–504, 1964.
- Zhang, Y., Gao, J.-F., Ma, D., and Pan, J.: The role of hydrothermal alteration in tungsten mineralization at the Dahutang tungsten deposit, South China, Ore Geol. Rev., 95, 1008–1027, 2018.
- Zhidikova, A. P. and Khodakovskiy, I. L.: Thermodynamic properties of ferberite, hubnerite, scheelite and powellite, in: *Physico-chemical models of petrogenesis and ore formation*, edited by: Tauson, L. V., Nauka, Novosibirsk, 145–156, 1984.